a

b ZFN1/2 reporter

ZFN3/4 reporter

c

Figure 2. Detection of ZFN-targeted deletion activity. (a) Schematic representation of the reporter plasmid used to detect the ability of ZFN to remove a DNA fragment flanked by two ZFN recognition sites. The expression of renilla luciferase (Rluc) is driven by the CMV promoter when the GFP expression cassette is removed by ZFN. The ZFN target sites are indicated by circles. pA is polyadenylation signal. (b) The ZFN1/2 or 3/4 reporter plasmids were transfected into 293 T cells in the presence of ZFN expression vectors as indicated in each panel. The cells were observed under a fluorescence microscope at a low magnification (× 100) at 2 days post transfection. (c) Transient transfection assay to assess the targeted deletion activity of ZFN. The ZFN expression vectors (500 ng; containing each subunit alone or equal amounts of each ZFN subunit) and the reporter plasmid (50 ng) were cotransfected into 293 T cells and the luciferase signals were detected at 2 days post transfection. A GFP expression vector was used as the control. Representative data from four independent experiments, each performed in triplicate, are shown. Significant differences between the ZFN pairs and the subunits alone were analyzed using a two-tailed Student's t-test (asterisk denotes P < 0.001).

Table 2. Cloning efficiency of HTLV-1-infected cells transduced with ZFN.

Cells	ZFN[a]	Cloning efficiency (%, mean ± s.d.)	Statistical significance
M8166	ZFN1 + ZFN2	0.14 ± 0.1 (N = 4)	
	ZFN2 + ZFN1	0.04 ± 0.05 (N = 4)	P = 0.0013, 26.9-fold, 8 vs 4
	ZFN1 + ZFN1	1.15 ± 0.15 (N = 2)	
	ZFN2 + ZFN2	3.75 ± 0.88 (N = 2)	
	ZFN3 + ZFN4	0.31 ± 0.15 (N = 2)	
	ZFN4 + ZFN3	0.36 ± 0.14 (N = 2)	P = 0.0018, 20.0-fold, 4 vs 5
	ZFN3 + ZFN3	4.38 ± 1.47 (N = 3)	
	ZFN4 + ZFN4	9.38 ± 0.88 (N = 2)	
S1T	ZFN1 + ZFN2	0.13 ± 0.02 (N = 2)	
	ZFN2 + ZFN1	0.11 ± 0.01 (N = 2)	P < 0.0001, 4.4-fold, 4 vs 4
	ZFN1 + ZFN1	0.51 ± 0.01 (N = 2)	
	ZFN2 + ZFN2	0.54 ± 0.13 (N = 2)	
	ZFN3 + ZFN4	0.35 ± 0.03 (N = 4)	
	ZFN4 + ZFN3	0.15 ± 0.04 (N = 2)	P = 0.08, 1.9-fold, 6 vs 6
	ZFN3 + ZFN3	0.41 ± 0.01 (N = 4)	
	ZFN4 + ZFN4	0.54 ± 0.02 (N = 2)	

Abbreviations: HTLV-1, human T-cell leukemia virus type 1; ZFN, zinc finger nuclease. [a]The order of transduction into cells is indicated.

Table 3. Detection of ZFN-mediated site-directed mutagenesis in S1T cells.

ZFN[a]	No. of clones examined	No. of clones with site-specific mutation
ZFN1 + ZFN2	9	3
ZFN2 + ZFN1	7	3
ZFN1 + ZFN1	1	0
ZFN2 + ZFN2	1	0
ZFN3 + ZFN4	12	4
ZFN4 + ZFN3	6	5
ZFN3 + ZFN3	3	0
ZFN4 + ZFN4	2	0

Abbreviation: ZFN, zinc finger nuclease. [a]The order of transduction into cells is indicated.

Reporter assay

Luciferase activity was measured 48 h after transfection or infection using a Dual-Glo or Renilla-Glo Luciferase assay kit (Promega, Madison, WI, USA) according to the manufacturer's protocol. Chemiluminescence was detected with a Veritas luminometer (Promega).

Immunoblotting

Western blotting and immunoprecipitation were performed as previously described[12] using an anti-FLAG antibody (F7425, Sigma) and Envision Dual Link System-HRP (Dako, Glostrup, Denmark). Chemiluminescence was generated using Lumilight (Roche) or Lumigen (GE Healthcare, Tokyo, Japan), and the signals were detected using an LAS-3000 mini Lumino-Image analyzer.

Cell proliferation assay

C8166 and S1T cells were transduced with ZFN genes inserted into the MLV vector and bulk-selected in medium containing 1 µg/ml puromycin. The cells were then transduced with a second ZFN gene in the MLV vector, seeded into 96-well plates (5 or 100 cells/well), and selected in medium containing 500 µg/ml G418 at 3 days post infection. The number of wells containing viable cells was counted at 3–4 weeks post selection. Cellular DNA was isolated using the Wizard DNA Purification Kit (Promega), and the proviral DNA sequence was analyzed by sequencing after PCR amplification of the target regions.

Mouse study

Balb/c nude Rag-2/Jak3 double-deficient (nude R/J) mice were established by crossing Balb/c nude mice and Balb/c Rag-2/jak3 double-deficient mice.[13] Nude R/J mice were inoculated subcutaneously in the right and left flanks with 2×10^5 ED$^{ZFN2/ZFN1}$ and ED$^{ZFN2/ZFN2}$ cells, respectively. Tumor growth was monitored at 6 weeks post inoculation by weekly measurement of the maximal and minimal diameter using calipers. Tumor size was estimated using the formula: tumor size (mm^3) = length (mm) × width^2 (mm) × 0.4.[14,15] The mice were housed and monitored in the animal research facility according to institutional guidelines. All experimental procedures and protocols were approved by the Institutional Animal Care and Use Committee at Kumamoto University (B23-201).

Statistical analysis

Experimental results were analyzed by Student's t-test, Person's exact test or Paired Wilcoxon Rank-Sum test, as appropriate. P < 0.05 were considered statistically significant.

RESULTS

We synthesized two pairs of ZFNs that targeted the HTLV-1 LTR, which are: ZFN1/2, which recognizes the R region (524–563 bp, according to the GenBank accession number D13784 coordinate) and ZFN3/4, which recognizes the U5 region (627–665 bp) (Figure 1a). According to our own data and the NCBI database, these sequences are conserved in 77.8% (14/18 clones) of independent HTLV-1 clones isolated in Asia, Europe, and North and South America. Sequence analysis indicated that the human genome does not contain sequences that are identical to these ZFN targets. ZFN was tagged at the N-terminus with a 3 × FLAG epitope and ZFN expression was verified by western blotting of 293 T cells transfected with the ZFN expression vectors (Figure 1b). As the ZFNs were fused to a nuclear localization signal, they were distributed predominantly in the nucleus (Figure 1c).

Next, ZFN activity was examined in human cells. First, we assessed whether ZFN inhibited LTR-driven gene expression. For this purpose, ZFN expression vectors were transfected into 293 T cells along with a Tax expression vector and a reporter plasmid encoding an HTLV-1 LTR-luciferase cassette. Luciferase activity was markedly reduced upon coexpression of functional ZFN pairs (Figure 1d). This effect was dependent upon the amount of plasmid transfected. By contrast, ZFN expression did not affect the transcriptional activity of the cytomegalovirus (CMV) promoter (Figure 1d). Second, two deletion reporter plasmids were constructed to test the targeted deletion activity. One deletion reporter harbored a CMV promoter and green fluorescent protein (GFP) and renilla luciferase genes (Figure 2a). The GFP gene was sandwiched by the cognate ZFN site (Figure 2a). The renilla luciferase was not expressed unless the GFP cassette was removed. The results of a cotransfection experiment in 293 T cells showed that GFP fluorescence decreased substantially in the presence of functional ZFN subunits (Figure 2b), whereas a marked increase in renilla luciferase activity was detected upon coexpression of functional ZFN subunits (Figure 2c).

To confirm this finding, we constructed another deletion reporter containing a bacterial LacZ-alpha expression cassette flanked by ZFN cognate sites and cotransfected it into 293 T cells with the ZFN expression plasmids. Escherichia coli were then transformed with DNA recovered from the transfected 293 T cells. Deletion of the LacZ-alpha expression cassette should result in white bacterial colonies on agar plates containing X-Gal. As expected, the number of white colonies increased substantially when the ZFN pairs were expressed in 293 T cells (Table 1). Interestingly, expression of the ZFN pairs caused a reduction in the number of colonies, suggesting that DSBs were efficiently introduced into the reporter plasmid, but not all of the DSB loci were ligated by the DSB repair system in 293 T
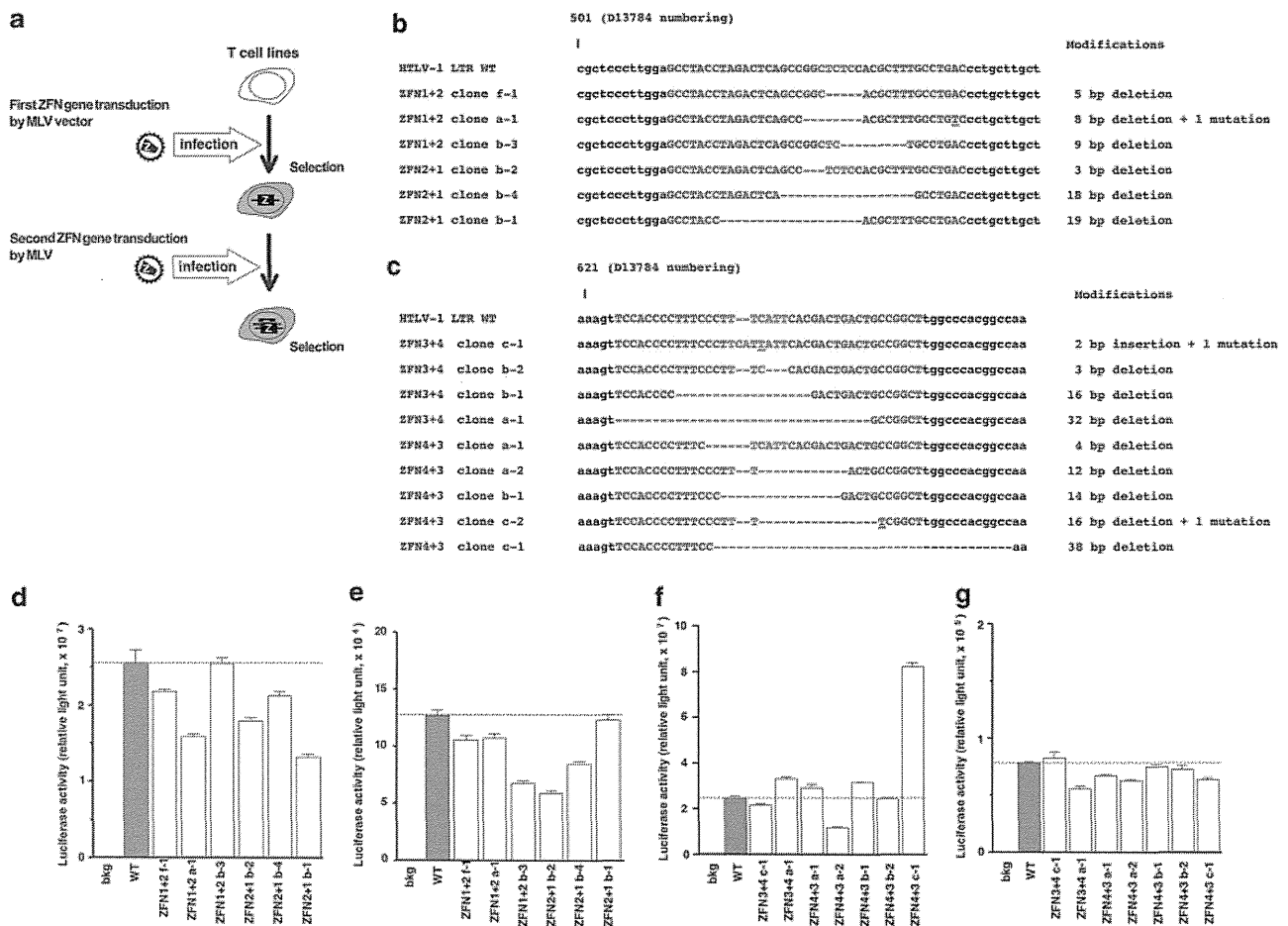
Figure 3. Effect of ZFN-mediated site-directed mutagenesis of the HTLV-1 LTR. (a) Experimental procedure used to assess the effect(s) of ZFN expression in HTLV-1-infected cells. (b and c) Sequence of the LTR (spanning the ZFN target sites) recovered from S1T cells transduced with ZFN1/ZFN2 (b) or ZFN3/ZFN4 (c). The nucleotide number coordinates are derived from GenBank accession number D13784. Blue letters represent the ZFN recognition sequence and red letters represent the DSB induction sites as in Figure 1a. Dashes represent deletions and underlining represents substitutions. (d–g) Reporter assay to assess the promoter activity of the LTR mutants shown in (b) and (c). The Tax expression vector (100 ng) and the reporter plasmid carrying the LTR mutants (200 ng) were cotransfected into 293 T cells and the luciferase signals were detected at 2 days post transfection. The transcriptional activity of the positive (d and f) and negative strand (e and g) is indicated. Data are representative of four independent experiments. The dashed line indicates the wild-type level.

cells. A small number of white colonies were observed, presumably because ZFN-independent deletion of LacZ from the reporter plasmid occurs spontaneously and with low frequency. Taken together, these data suggest that ZFNs inhibit the function of the LTR promoter and remove DNA flanked by the ZFN cognate sites. We assume that the inhibition of LTR promoter function (Figure 1d) was caused by physical damage to the LTR.

We next examined the biological effect(s) of ZFNs in HTLV-1-transformed and ATL-derived CD4-positive human T-cell lines, harboring the HTLV-1 provirus. HTLV-1 immortalizes human CD4-positive T cells, and the proliferation of HTLV-1-transformed cells is dependent on HTLV-1 gene expression. If ZFN inhibits the promoter function of the LTR, then ZFN expression should inhibit the proliferation of HTLV-1-transformed cell lines. In addition, HTLV-1-positive cells should undergo DSB-triggered apoptosis upon ZFN expression. We confirmed that the ZFN target sequence in the LTR was conserved in all the cell lines used in this study. Initially, we transduced a subunit of ZFN into C8166 cells[16] using a MLV vector. A second ZFN subunit was then transduced into the cells using a MLV vector carrying a distinct selection marker, and cell proliferation was examined by measuring the cell-cloning efficiency (Figure 3a). For the control cells, the same ZFN subunit

that was transduced initially was introduced again (referred to as a "non-functional pair"). When the functional ZFN1/2 and ZFN3/4 pairs were expressed, the cloning efficiency of C8166 cells was significantly reduced by 26.9- and 20.0-fold, respectively, compared with that of the control ($P = 0.001$ and $P = 0.002$, respectively; Student's t-test, Table 2). Next, we examined the ATL cell line S1T, which proliferates in an interleukin-2-independent manner.[17] Under the same experimental conditions, the cloning efficiency of S1T cells was reduced by 4.4- and 1.9-fold compared with the control when functional ZFN1/2 and ZFN3/4 pairs, respectively, were expressed (Table 2). The reduction in the cell-cloning efficiency mediated by ZFN1/2 (but not ZFN3/4) was statistically significant ($P < 0.001$; Student's t-test). Proliferative inhibition of HTLV-1-transformed and ATL-derived cell lines was observed when cell growth was assessed in bulk culture using metabolic measurements (data not shown). We observed similar results in HTLV-1-transformed MT-2 and MT-4 cells, and the ATL-derived cell lines, ED and TL-Oml (data not shown). Furthermore, these findings were not observed in four HTLV-1-negative CD4-positive T-cell lines, including CEM, MOLT-4, Jurkat and SUP-T1 (data not shown). These data suggest that ZFN inhibits the proliferation of HTLV-1-infected cells, specifically. We also noted that the cell-cloning efficiency was reduced to a greater extent in
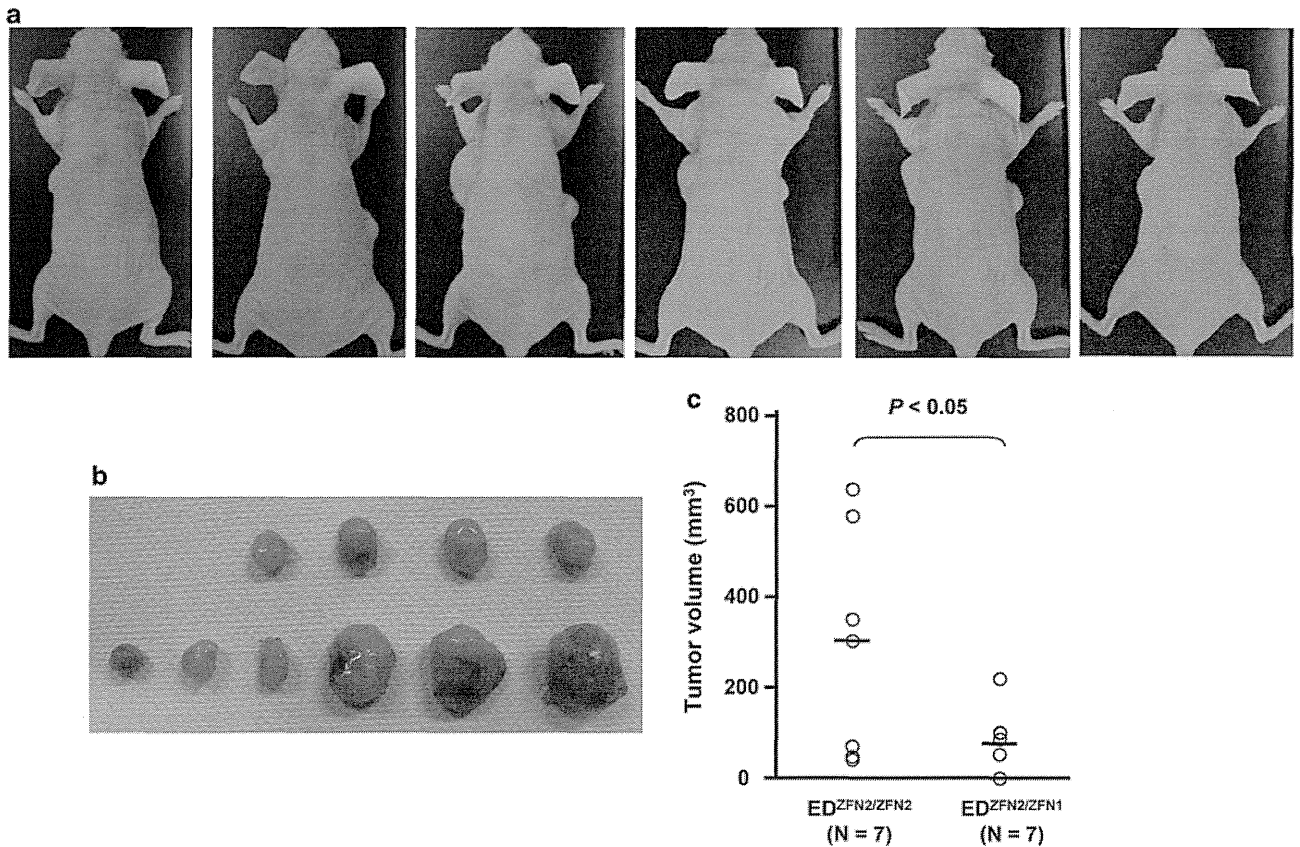
Figure 4. ZFN-mediated inhibition ATL cell tumorigenesis *in vivo*. (a) Engraftment of ED cells transduced with ZFNs into Balb/c nude Rag-2/Jak3 double-deficient (nude R/J) mice. ED$^{ZFN2/ZFN1}$ and ED$^{ZFN2/ZFN2}$ cells were transplanted into the left and right flanks, respectively. Mice were photographed at 6 weeks post-cell inoculation. (b) Nude R/J mice were killed at 6 weeks post-cell inoculation. The tumors were dissected, photographed and measured. (c) The estimated tumor volume is shown. The bar represents the average of the group. Significant differences between the two groups were analyzed using the paired Wilcoxon Rank-Sum test ($P < 0.05$).

HTLV-1-transformed cells than in ATL-derived cells. Presumably, this is because HTLV-1-transformed cells are more susceptible to DSB-induced apoptosis.

Next, the physical damage to the LTR sequence caused by ZFN was examined in S1T cell clones recovered from the above experiment. We identified site-specific mutations in 44.1% (15/34 clones) of LTR sequences derived from S1T cell clones, expressing functional ZFN pairs, whereas no mutations were found in LTR clones isolated from the controls (0/7 clones, $P < 0.05$; Pearson's exact test, Table 3). Most of the mutations were deletions (average, 14.1 bp/clone). Expression of ZFN3/4 resulted in larger deletions (15.0 bp/clone) than expression of ZFN1/2 (10.2 bp/clone). An insertional mutation was detected only in a single ZFN3/4-transduced clone (2 bp, 2.9%, 1/34 clones; Figures 3b and c). These data suggest that DSB repair occurs in ATL cells, but that the quality of the repair at the ZFN1/2 and ZFN3/4 sites is different. We assume that clones bearing a wild-type LTR might have failed to express ZFNs efficiently, or lost ZFN expression during selection.

The promoter activity of some LTR mutants was examined in a reporter assay in which the reporter plasmid contained both firefly and renilla luciferases, representing positive and negative strand transcription, respectively (Figure 3d–g). The Tax-augmented transcription of the positive strand was reduced by most of the mutations introduced by ZFN1/2 (4/6 clones, Figure 3d). Similarly, the negative strand transcription was also reduced by ZFN1/2-induced mutations (5/6 clones, Figure 3e). On the other hand, increased positive strand transcription was observed in 4/7 LTR mutants recovered from ZFN3/4-transduced cells (Figure 3f).

By contrast, many of the LTR mutants showed modestly reduced negative strand transcription (Figure 3g). Sequence analysis suggested that the LTR sequences targeted by ZFNs do not contain binding sites for previously-known transcription factors; therefore, it is possible that the ZFN1/2 target site spans a cis-acting element that supports the efficient transcription of the positive strand. All S1T cell clones were positive for the *gag* gene, suggesting that removal of the entire proviral genome was inefficient, or that ATL cells cannot proliferate without the provirus. However, some S1T cell clones showed reduced gag-to-LTR ratios as measured by quantitative real-time PCR, suggesting that removal of some proviral gene copies is possible (data not shown). Taken together, these data suggest that ZFN-mediated killing of S1T cells is not because of the loss of viral genes, but more likely due to DSB-induced apoptosis.

To evaluate the potential of ZFN1/2 to inhibit tumorigenicity of ATL cells *in vivo*, we adopted ATL cell xenograft model in Balb/c nude Rag-2/Jak3 double-deficient (nude R/J) mice. We chose to use ED cells because they form a tumor mass in nude mice and do not require human interleukin-2 for growth.[18] In addition, ED cells are highly susceptible to infection by MLV vectors. As shown above, the biological effect of ZFN1/2 was greater than that of ZFN3/4 in both HTLV-1-transformed and ATL-derived cell lines. Therefore, we used the ZFN1/2 pair for the *in vivo* study. ED cells constitutively expressing ZFN2 (ED^{ZFN2}) were infected with MLV vectors, harboring *GFP*, *ZFN1* or *ZFN2* gene (Figure 3a). Approximately half of the cells were infected by the MLV vectors as estimated by the number of GFP-positive cells (data not shown). Cells were inoculated intradermally into into nude mice at

2 days post-MLV infection. ED$^{ZFN2/ZFN1}$ cells showed a lower rate of tumor formation, and the tumors were significantly smaller than those in control mice (Paired Wilcoxon Rank-Sum test, $P < 0.05$; Figure 4). These data indicate that ZFN1/2 shows promising therapeutic efficacy against ATL.

DISCUSSION

We synthesized two pairs of ZFNs that successfully targeted the HTLV-1 proviral LTR and inhibited the proliferation of HTLV-1-transformed and ATL-derived T-cell lines. ZFN caused physical damage to the LTR and disrupted its function. Even though some cells survived, they contained a defective provirus; therefore, the therapeutic effects should be long-lasting. ZFN was able to remove at least a part of proviral genes from HTLV-1-infected cells and showed anti-tumor effects in vivo. Taken together, these data show that ZFN is an attractive therapeutic molecule for treating HTLV-1 infection, and may form the basis of a treatment that eliminates the virus from infected cells. Previous studies used ZFN to edit the human genome.[19,20] However, the work reported herein is unique in that ZFN was used to kill target cells via DSB-triggered apoptosis. This approach can be used for other viruses that establish latent infections and are associated with human malignancies, including retroviruses, Epstein-Barr virus, Kaposi sarcoma herpes virus, papilloma virus and hepatitis B virus.

The choice of a viral vector may improve the efficacy of ZFN in terms of limiting the proliferation of HTLV-1-infected cells. We delivered the ZFN gene using an MLV vector; however, adenoviral vectors have been used for the clinical application of ZFNs.[20] The advantage of an adenoviral vector is that it induces transient, but high levels of ZFN expression, whereas retroviral vectors express the gene of interest constitutively, but at low levels. We found that ZFN expression in cells gradually decreased after the long-term cultivation, as is often the case with other genes. This suggests that MLV-mediated gene transduction may not be appropriate for clinical application. We also expect that ZFN-mediated cell killing can be enhanced by inhibiting DSB repair proteins, a method used to increase the efficacy of DNA-damaging agents against tumor cells.[21]

The major hurdle that must be overcome if ZFNs are to be used clinically to treat HTLV-1 infection is their efficient delivery to virus reservoirs. To eliminate HTLV-1 from infected individuals, ZFN must be delivered directly to latently infected cells; however, the latent reservoir of HTLV-1 is poorly understood. Although ZFN has a high-substrate specificity and its non-specific effects are thought to be minimal, delivery of ZFN to all the cells may not be desirable. Cell surface markers of HTLV-1-infected cells, either transformed or not, remain to be identified. We must increase our understanding of HTLV-1 latency if we are to use ZFNs in a clinical setting. Off-target effects are another concern. Although ZFN did not inhibit the proliferation of HTLV-1-negative cells, the risk that ZFNs may edit the human genome must be addressed in future studies. Phase I and II clinical trials using ZFN to treat human immunodeficiency virus infection and recurrent/refractory malignant glioma are currently underway (NCT00842634, 01044654, and 01082926), suggesting that the clinical application of ZFN is feasible. Another issue to be addressed is the stage of HTLV-1 infection at which ZFN should be used; for example, during the latent period or after the onset of HTLV-1-associated disease.

AUTHOR CONTRIBUTIONS

AT, ST, EU, RK, KM, SO and JK planned and performed the experiments, and analyzed the data. AT, ST, SO and JK wrote the manuscript.

REFERENCES

1 Nagai M, Osame M. Human T-cell lymphotropic virus type I and neurological diseases. J Neurovirol 2003; 9: 228–235.
2 Watanabe T. HTLV-1-associated diseases. Int J Hematol 1997; 66: 257–278.
3 Yasunaga J, Matsuoka M. Molecular mechanisms of HTLV-1 infection and pathogenesis. Int J Hematol 2011; 94: 435–442.
4 Faris M. Potential for molecular targeted therapy for adult T-cell leukemia/lymphoma. Int Rev Immunol 2008; 27: 71–78.
5 Taylor GP, Matsuoka M. Natural history of adult T-cell leukemia/lymphoma and approaches to therapy. Oncogene 2005; 24: 6047–6057.
6 Carroll D. Progress and prospects: zinc-finger nucleases as gene therapy agents. Gene Ther 2008; 15: 1463–1468.
7 Cannon P, June C. Chemokine receptor 5 knockout strategies. Curr Opin HIV AIDS 2011; 6: 74–79.
8 Handel EM, Cathomen T. Zinc-finger nuclease based genome surgery: it's all about specificity. Curr Gene Ther 2011; 11: 28–37.
9 Onishi M, Kinoshita S, Morikawa Y, Shibuya A, Phillips J, Lanier LL et al. Applications of retrovirus-mediated expression cloning. Exp Hematol 1996; 24: 324–329.
10 Kawakami Y, Miura T, Bissonnette R, Hata D, Khan WN, Kitamura T et al. Bruton's tyrosine kinase regulates apoptosis and JNK/SAPK kinase activity. Proc Natl Acad Sci USA 1997; 94: 3938–3942.
11 Komano J, Miyauchi K, Matsuda Z, Yamamoto N. Inhibiting the Arp2/3 complex limits infection of both intracellular mature vaccinia virus and primate lentiviruses. Mol Biol Cell 2004; 15: 5197–5207.
12 Shimizu S, Urano E, Futahashi Y, Miyauchi K, Isogai M, Matsuda Z et al. Inhibiting lentiviral replication by HEXIM1, a cellular negative regulator of the CDK9/cyclin T complex. AIDS 2007; 21: 575–582.
13 Ono A, Hattori S, Kariya R, Iwanaga S, Taura M, Harada H et al. Comparative study of human hematopoietic cell engraftment into BALB/c and C57BL/6 strain of rag-2/jak3 double-deficient mice. J Biomed Biotechnol 2011; 2011: 539748.
14 Attia MA, Weiss DW. Immunology of spontaneous mammary carcinomas in mice. V. Acquired tumor resistance and enhancement in strain A mice infected with mammary tumor virus. Cancer Res 1966; 26: 1787–1800.
15 Harada H, Suzu S, Ito T, Okada S. Selective expansion and engraftment of human CD16+ NK cells in NOD/SCID mice. Eur J Immunol 2005; 35: 3599–3609.
16 Salahuddin SZ, Markham PD, Wong-Staal F, Franchini G, Kalyanaraman VS, Gallo RC. Restricted expression of human T-cell leukemia–lymphoma virus (HTLV) in transformed human umbilical cord blood lymphocytes. Virology 1983; 129: 51–64.
17 Hsu DK, Hammes SR, Kuwabara I, Greene WC, Liu FT. Human T lymphotropic virus-I infection of human T lymphocytes induces expression of the beta-galactoside-binding lectin, galectin-3. Am J Pathol 1996; 148: 1661–1670.
18 Okada M, Maeda M, Tagaya Y, Taniguchi Y, Teshigawara K, Yoshiki T et al. TCGF(IL 2)-receptor inducing factor(s). II. Possible role of ATL-derived factor (ADF) on constitutive IL 2 receptor expression of HTLV-I(+) T cell lines. J Immunol 1985; 135: 3995–4003.
19 Perez EE, Wang J, Miller JC, Jouvenot Y, Kim KA, Liu O et al. Establishment of HIV-1 resistance in CD4+ T cells by genome editing using zinc-finger nucleases. Nat Biotechnol 2008; 26: 808–816.
20 Holt N, Wang J, Kim K, Friedman G, Wang X, Taupin V et al. Human hematopoietic stem/progenitor cells modified by zinc-finger nucleases targeted to CCR5 control HIV-1 in vivo. Nat Biotechnol 2010; 28: 839–847.
21 Willmore E, de Caux S, Sunter NJ, Tilby MJ, Jackson GH, Austin CA et al. A novel DNA-dependent protein kinase inhibitor, NU7026, potentiates the cytotoxicity of topoisomerase II poisons used in the treatment of leukemia. Blood 2004; 103: 4659–4665.

Supplementary Information accompanies this paper on the Leukemia website (http://www.nature.com/leu)

Influence of Lipid Composition on the Structural Stability of G-Protein Coupled Receptor

Md. Iqbal Mahmood, Xinli Liu, Saburo Neya, and Tyuji Hoshino*

Graduate School of Pharmaceutical Sciences, Chiba University; 1–8–1 Inohana, Chuo-ku, Chiba 260–8675, Japan.
Received December 12, 2012; accepted January 20, 2013

β_2 Adrenergic receptor (β_2AR) is a kind of G-protein coupled receptors (GPCRs) which transduce a wide range of extracellular signals into intracellular messages responsible for the regulation of diverse cell functions. Because of their functional ubiquity, GPCR is one of the most important drug targets in pharmaceutical industry. Although recent crystallographic studies provided both the active and the inactive states of some families of GPCRs, the influence of lipid composition of bilayer membrane on their activation is still poorly understood. In this work, we address the influence of lipid composition on the structural stability of GPCR, performing molecular dynamics simulations of three kinds of states: apo-, and agonist epinephrine-, or antagonist alprenolol-bound β_2AR. These three kinds of β_2ARs were embedded in four types of lipid membranes: (i) pure palmitoyl-oleoyl-phosphatidyl-choline (POPC), (ii) POPC/cholesterol (CHL), (iii) POPC/CHL/GM1 (GM1 ganglioside), (iv) POPC/palmitoyl-oleoyl-phosphatidyl-ethanolamine (POPE)/CHL/ sphingomyeline (SM). The side chains of Lys267$^{6.29}$ and Asp331$^{7.58}$ showed different conformations among the three states in all types of lipid membranes. The distances between Lys267$^{6.29}$ and Asp331$^{7.58}$ of apo- and alprenolol-bound β_2ARs are smaller than that of the epinephrine-bound β_2AR. In contrast, β_2ARs in POPC/ CHL bilayer were unstable in which the salt bridge; i.e., ionic lock, was not formed between Arg131$^{3.50}$ and Glu268$^{6.30}$. We have also examined the distribution of lipid molecules. A stable hydrophobic interaction between CHL and β_2AR was observed at transmembrane helix5 in POPC/CHL/GM1 and POPC/POPE/CHL/ SM membranes. These results suggest that the lipid composition strongly affects the conformation of GPCR and essentially concerns the GPCR activation.

Key words   G-protein coupled receptor; β_2 adrenergic receptor; lipid bilayer; molecular dynamics simulation

G-Protein coupled receptors (GPCRs) are the largest class of versatile signaling molecules that are responsible for the signal transduction across cellular membranes in response to extracellular hormones or neurotransmitters, *etc.*[1] Accordingly, GPCRs have been the major drug targets in pharmaceutical industry. The β_2 adrenergic receptor (β_2AR) is well studied member of GPCR families, which mediates the effects of catecholamine, epinephrine, and norepinephrine.[2] β_2AR plays an important regulatory role in a variety of cells and organs and is an important therapeutic target in the treatment of airway and cardiovascular disease.[3] Like other GPCRs, the conformation of β_2AR is known to vary between the inactive and the active states. The conformational change induced by the binding of extracellular ligands to β_2AR results in the G-protein-mediated cell signaling.

The protein structures vary, depending on the inactive and the active signaling state of the receptor. The crystal structures of two GPCRs, β_2AR and bovine rhodopsin, have recently been revealed both for the active state (agonist-bound) and the inactive state (antagonist-bound).[4–6] The human β_2AR is one of the first GPCRs to be identified through ligand binding, and is the first neurotransmitter receptor to be cloned.[7] Its structure has been determined in complex with various kinds of ligands including inverse agonists, full agonists, and antagonists.[8–10] In the previous computational studies, the inactive state of β_2AR in complex with agonist or antagonist has been embedded in a lipid bilayer membrane composed of a single type of lipid molecule (palmitoyl-oleoyl-phosphatidyl-ethanolamine (POPE) bilayer or palmitoyl-oleoyl-phosphatidyl-choline (POPC) bilayer).[6,11] Recent studies suggest that

rafts, special kind of micro-domains that are enriched by cholesterol (CHL), play an essential role in the signaling by enabling the conformational change of GPCRs.[12–16] In the present study, we analyze the inactive structure of β_2AR without ligand (apo) or in complex with ligand (agonist epinephrine and antagonist alprenolol) embedded in the palmitoyl-oleoyl-phosphatidyl-choline (POPC) bilayer, cholesterol (CHL) containing POPC, GM1 ganglioside containing POPC/CHL, or the mixed membrane consisting of POPC, palmitoyl-oleoyl-phosphatidyl-ethanolamine (POPE), CHL, sphingomyeline (SM). The last one imitates the biological membranes, using a software program developed for modeling various types of lipid membranes.[17] The mixed membrane, POPC/POPE/CHL/ SM, was created referring the studies on the lipid composition of biological membrane.[18–21] In erythrocyte, the lipid bilayer was composed of equal ratios by weight of cholesterol (CHL) and phospholipids.[19] The three major phospholipids are POPC, POPE and SM.[19,21] About 25% of the phospholipids is SM.[21] Judging from these findings, 50% of the POPC/POPE/CHL/ SM mixed membrane was set to CHL. SM was included at 12% in the mixed membrane. POPC and POPE were assigned to the rest 38%. Therefore, our simulation using the membrane model with the mixed lipid composition will be helpful to understand the structural perturbation of GPCRs in the biological membrane.

In the diverse intracellular signaling process, β_2ARs constitute multiple receptor conformation in its active and inactive states. Biochemical and biophysical studies suggested that the rearrangement of helix3 and helix6 was involved in the activation process of rhodopsin and β_2AR.[22–24] Moreover the inactive rhodopsin structures demonstrated that highly conserved residue Arg131$^{3.50}$ (superscripts refer to Ballesteros–Weinstein

---

* To whom correspondence should be addressed.   e-mail: hoshino@chiba-u.jp

residue numbering scheme[25]) at the end of intracellular part of helix3 formed a salt bridge; *i.e.*, ionic lock, with acidic residue Glu268$^{6.30}$ at the end of intracellular part of helix6.[26–28] In contrast, an activated rhodopsin structure showed the break of the ionic lock between Arg131$^{3.50}$ and Glu268$^{6.30}$.[22,23,29,30] Although the crystal structure of the inactive β_2AR lacks the salt bridge between Arg131$^{3.50}$ and Glu268$^{6.30}$, several biochemical studies have suggested that an ionic lock between Arg131$^{3.50}$ and Glu268$^{6.30}$ is established in β_2AR as well as other GPCRs.[6,31–35] The disruption of ionic interaction between the highly conserved D(E)RY residue at helix3 and an acidic residue at helix6 is considered to promote the receptor activation and to be highly related to the conformational change of both rhodopsin and β_2AR.[22,31,35]

For understanding of the activation mechanism of β_2AR embedded in a lipid bilayer membrane, in this work, we have performed molecular dynamics (MD) simulation by constructing computational models for ligand bound and unbound β_2AR embedded in four types of lipid bilayer membranes; pure POPC, POPC/CHL, POPC/CHL/GM1 and POPC/POPE/SM/CHL, solvated with water molecules, and executed 100 ns MD simulations for every model system with applying periodic boundary conditions. We particularly address the effect of lipid composition of bilayer membrane on the ligand bound and unbound β_2AR receptor. Several huge MD simulations previously characterized the dynamics of rhodopsin and/or β_2AR and some simulation studies on β_2AR mainly focused on the formation of ionic lock.[6,36–40] Contrary to the huge simulations, a few reports[14,15,41] have indicated that lipid composition modulates the activity of GPCRs. In MD simulations of two kinds of GPCRs of k-opioid receptor and rhodopsin in CHL-depleted and CHL-enriched model membranes, k-opioid receptor was suggested to functionalize better in CHL-enriched environments, while a relatively low concentration of CHL was favorable for rhodopsin.[41] Therefore, GPCR function is closely linked to the composition of lipid membrane and CHL will highly affect the functional motion or conformational change of GPCRs.[14,15,42–44] In the study of k-opioid receptor and rhodopsin, the DMPC/CHL bilayer was employed with setting the ratio of CHL 20%.[41] In our POPC/CHL, POPC/CHL/GM1 and POPC/POPE/SM/CHL models, CHL was set to be about 50% of lipid molecules. Accordingly the amount of cholesterol is assumed to be sufficient to observe the β_2AR activation.

In this study, MD simulations using the membrane models with different kind of lipid compositions showed the change in the ionic lock formation between Arg131$^{3.50}$ and Glu268$^{6.30}$ in *apo-*, epinephrine- and alprenolol-bound β_2AR. We compared these results to the previous study performed using pure lipid bilayer POPE.[6] The previous study showed that the ionic lock was formed in *apo-* and inverse agonist carazolol-bound β_2AR. Our simulations with pure POPC and POPC/POPE/CHL/SM membranes were consistent with the previous study. Our simulation further suggested that the receptor in *apo-* and epinephrine- or alprenolol-bound form hardly maintained the ionic lock in POPC/CHL bilayer. This means that the composition of lipid membrane is essentially important for the activation of GPCR. One of the lipid components; CHL, has been observed to strongly interact with the receptor in the POPC/CHL/GM1 and POPC/POPE/CHL/SM mixed membrane. The present computational study will clarify the complex structure

of GPCR and CHL and enhance the understanding of the influence on the receptor function.

Experimental

The initial structure of β_2AR receptor for MD simulations was taken from an X-ray crystal structure of the carazolol-bound β_2AR/T4-lysozyme fusion protein (code 2RH1) solved by Cherezov *et al.*[45] The lysozyme and ligand carazolol were removed. The N-terminal 35 residues did not appear in the crystal structure. Hence, the missing residues were not included in our model of β_2AR receptor. The protonation states of charged residues and histidines were determined on the basis of pK_a values calculated by PROPKA.[46] According to the PROPKA calculation results, the δ nitrogen atoms in His93, 172, 178, 269 and 296 were set to be protonated and the ε nitrogen atoms were deprotonated for those residues.

The full agonist epinephrine was manually docked into the β_2AR and the neutral antagonist alprenolol was also docked to the β_2AR, referring the crystal structure of ligand-bound β_2AR (PDB code 3NYA).[9] The chemical structures were subjected to geometrical optimization at the B3LYP/6-31G** level using Gaussian03 software. Atomic charges of the chemicals were determined by the restrained electrostatic potential (RESP) fitting procedure[47] using the optimized structure. The force field parameters for epinephrine and alprenolol were determined by parameterizing fragment molecules and combining them according to the CHARMM parameterization methodology. The CHARMM force field for small organic molecules[48] and the CHARMM27 force fields for lipids[49] were employed for all simulation. All of the bilayer models were constructed using VMD ver. 1.8[50] and an in-house program named GLYMM which is a VMD plug-in to add a function of automatically making a heterogeneous lipid bilayer.[17] Initially, the coordinates of all lipids were generated by the membrane tool of VMD, which provided the atom geometry of the liquid crystalline state of POPC lipids. Next, some of POPC molecules were converted into POPE, SM, CHL, or GM1 by GLYMM. The missing parameters were already created based on the analogy with available parameters.[51] The POPC bilayer model consisted of 226 POPC molecules. The POPC/CHL bilayer consisted of 120 POPC and 112 CHL molecules (POPC/CHL=0.52:0.48). The POPC/CHL/GM1 bilayer consisted of 128 POPC, 104 CHL and 7 GM1 molecules (POPC/CHL/GM1=0.54:0.43:0.03). The POPC/POPE/SM/CHL bilayer consisted of 36 POPC, 58 POPE, 112 CHL and 26 SM molecules (POPC/POPE/CHL/SM=0.15:0.25:0.48:0.12). Hence, calculation models in this work provided various types of membrane environments in which β_2AR receptor were placed. TIP3P water molecules and ions to neutralize the calculation cell were generated to solvate the complex of β_2AR and lipid membrane, making a periodic boundary box of *ca.* 80 Å×90 Å×120 Å. Consequently, the total number of atoms was approximately 75000 in each model as shown in Fig. 1a.

MD simulations were carried out for every model using NAMD ver. 2.7[52] under the isothermal–isobaric (NPT) ensemble condition. The simulations were divided into four parts: minimization, heating, equilibration, and production runs. After the potential energy had been minimized, the model system was heated to 310 K with z coordinates of the head groups of the lipids restrained in order for the lipids to move only in the x and y directions. Gradually releasing the
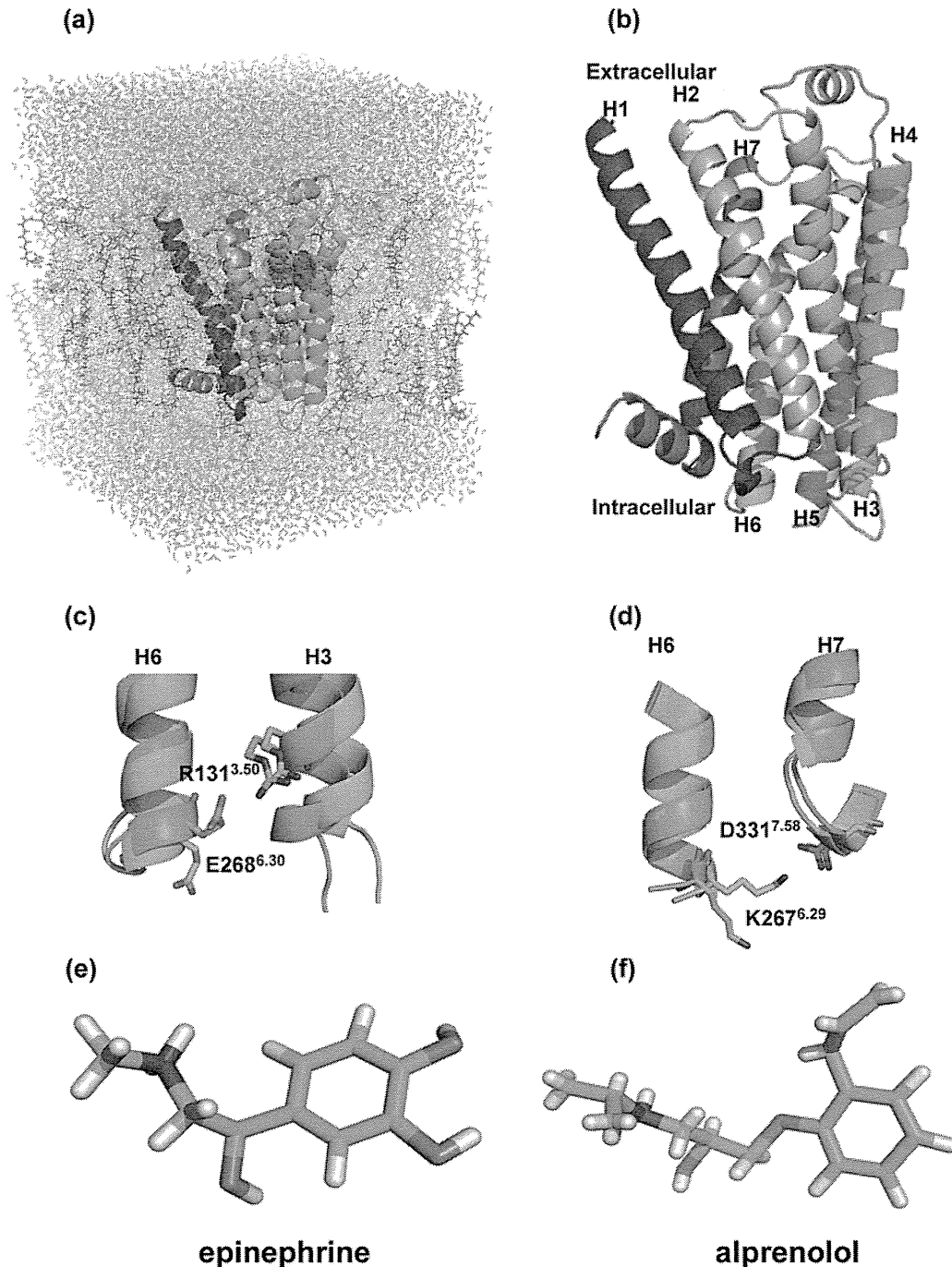
(a)

(b)

Extracellular

H1 H2

H7 H4

Intracellular H6 H5 H3

(c)

H6 H3

R131$^{3.50}$

E268$^{6.30}$

(d)

H6 H7

D331$^{7.58}$

K267$^{6.29}$

(e)

(f)

epinephrine **alprenolol**

Fig. 1. (a) Computational Model of β_2AR Embedded in a Lipid Membrane with Water Layer

(b) Conformation of seven transmembrane helices of β_2AR extracted from a crystal structure; PDB code: 2RH1. (c) Intracellular ends of helix3 and helix6. The structure keeping the ionic lock is shown in green and that without maintaining the ionic lock is in cyan. (d) Intracellular ends of helix6 and helix7. The side chains of Lys267$^{6.29}$ and Asp331$^{7.58}$ in the agonist-bound state is colored green and that of the antagonist-bound state is cyan. Structures of (e) agonist epinephrine and (f) antagonist alprenolol. (Color images were converted into gray scale.)

restraint, we equilibrated the system at a constant temperature of 310 K and a constant pressure of 1 atm and then carried out production runs under no restraint condition. The simulation times for equilibration and production runs were 10 ns and 100 ns, respectively. Non-bonded interaction terms were computed with a cutoff distance of 12 Å, where a switching distance of 10 Å was applied to make the non-bonded interaction zero at the cutoff distance smoothly. An integration time step was 2 fs. A periodic boundary condition was applied to all directions of the calculation cell in a similar manner to

the previous work,[53] and the particle mesh Ewald method was employed to compute the long-distance non-bonded interaction. CHARMM27 force field[49] was adopted for all the atoms except for ligand chemical.

The root mean square deviation (RMSD) measurement was performed, using the ptraj module of AMBER11.[54] In this analysis, only the coordinates for C, O, and N atoms of the main chain of receptor were used, because the flexibility of the side chain is large. The trajectories acquired from the 100 ns MD simulation were fit to the snapshot structure after

the 10 ns equilibration run as a reference. The average structure was calculated using the trajectories for the last 20 ns, because the RMSD showed small values for the last 20 ns in MD simulation.

Fluctuation of main chain atoms for the respective residues of the receptor was examined using the trajectories for 100 ns of the MD simulation. Fluctuation was evaluated by the B-factor values[55,56] calculated by the ptraj module of AMBER11 without including side chain. The structure after equilibration was used as the reference, and the trajectories were fit to this reference with respect to C, O, and N atoms in the main chain to eliminate the movement due to the rotation and the transversal motions.

The C_α–C_α and N–O distances shown in Fig. 4 were computed from the snapshot structures of the 100 ns MD simulation. We focused on two major conformational changes in which one is the inactive; ionic lock is formed, and another is the active state; ionic lock is broken, as shown in Fig. 1c. The N–O and C_α–C_α distances regarding to the ionic lock were measured to examine whether the ionic lock is formed or broken between Arg131[3.50] and Glu268[6.30]. Another distance between Lys267[6.29] of intracellular end of helix6 and Asp331[7.58] of intracellular end of helix7 was also measured with respect to C_α–C_α and N–O distances as shown in Fig. 1d.

The distribution of lipid molecules around β_2AR was measured with respect to their distance and direction and was visualized using gnuplot. Each coordinate of lipid molecule in the respective trajectories was rotated and superimposed so that β_2AR were fitted to the reference one.

Results

We carried out 12 patterns of 100 ns MD simulations for β_2AR embedded in pure and/or mixed membrane bilayers as shown in Table 1. The crystal structure of β_2AR; PDB code: 2RH1, shown in Fig. 1b was used for the receptor. For the ligand-free, apo form, the simulations are labeled as a, b, c and d. An agonist epinephrine (Fig. 1e) was docked into the binding pocket manually referring to the literature,[57,58] and the simulations are labeled as a', b', c' and d'. An antagonist alprenolol (Fig. 1f) was placed at the binding site, referring the crystal structure; PDB code: 3NYA,[9] and the simulations are labeled as a", b", c" and d". The simulations using pure POPC bilayer were labeled as a, a' and a". POPC bilayer containing CHL was used in simulations b, b' and b". POPC, CHL and GM1-ganglioside containing membrane was used

in simulations c, c' and c". The mixed membrane consisting of POPC, POPE, CHL and SM was used in simulations d, d' and d".

Fluctuation of Protein Residues Fluctuation of protein structure is closely related to the stability of protein. Flexibility of protein was highly correlated with protein functions.[59] B-factor analysis presents the deviation of atom positions from their average points. The calculated B-factor values of β_2AR for the respective models are shown in Fig. S1 of Supplementary Information. A comparison among simulations a, a' and a" suggested that, in POPC bilayer, the flexibility of protein residues in apo form was higher than those in the presence of epinephrine and alprenolol, and simulation a" gave the smallest fluctuation (Fig. 2a). Therefore, alprenolol stabilized the β_2AR structure. The flexibility of protein residues for POPC/CHL bilayer model was significantly decreased compared to that of pure POPC bilayer (Fig. 2b). Simulations for POPC/CHL/GM1 and mixed POPC/POPE/CHL/SM bilayers showed further small flexibility compared with the pure POPC and POPC/CHL bilayer (Figs. 2c, d). In the presence of alprenolol, simulations always showed the small flexibility for protein residues than other simulations. These results suggest that the lipid molecule strongly influences the stability of the residues and alprenolol also affects the flexibility of the receptor.

Binding Structure Figures 3a and b show the superimposition of the average structures of simulations for epinephrine-bound and alprenolol-bound β_2ARs to the apo-β_2AR in the POPC/POPE/CHL/SM mixed membrane (simulations d, d', d"). The averaged structures were obtained from the last 20 ns MD simulations (Fig. S2) and pymol software[60] were employed to superimpose the structures with respect to main chain atoms of β_2AR. β_2AR is bound to Gα protein with making hydrogen-bond network between them, in which Thr68[2.39], Asp130[3.49] and Arg131[3.50] of β_2AR are strongly involved in the binding.[61] The comparison of β_2AR structures among simulations d, d' and d" indicated that the Gα binding site kept the almost similar conformation as shown by blue mesh in Figs. 3a and b. To analyze the interactions between ligands and β_2AR receptor in all the models (Figs. S3, S4), we evaluated the hydrogen-bond network connecting ligand and β_2AR. In the presence of epinephrine (Fig. 3c, Figs. S3, S4), epinephrine interacted with Ser203[5.42], Ser207[5.46] and with Asp113[3.32] of β_2AR. The movement of helix5, which has also been investigated in the recently published crystal structures of β_2AR,[4,10,61] is important for forming the hydrogen-bond

Table 1. Calculation Pattern of the MD Simulations

| Simulation	Components of lipid bilayer	Protein	Ligand	Simulation time (ns)
a	POPC	β_2AR	—	100
a'	POPC	β_2AR	Epinephrine	100
a"	POPC	β_2AR	Alprenolol	100
b	POPC/CHL	β_2AR	—	100
b'	POPC/CHL	β_2AR	Epinephrine	100
b"	POPC/CHL	β_2AR	Alprenolol	100
c	POPC/CHL/GM1	β_2AR	—	100
c'	POPC/CHL/GM1	β_2AR	Epinephrine	100
c"	POPC/CHL/GM1	β_2AR	Alprenolol	100
d	POPC/POPE/SSM/CHL	β_2AR	—	100
d'	POPC/POPE/SSM/CHL	β_2AR	Epinephrine	100
d"	POPC/POPE/SSM/CHL	β_2AR	Alprenolol	100
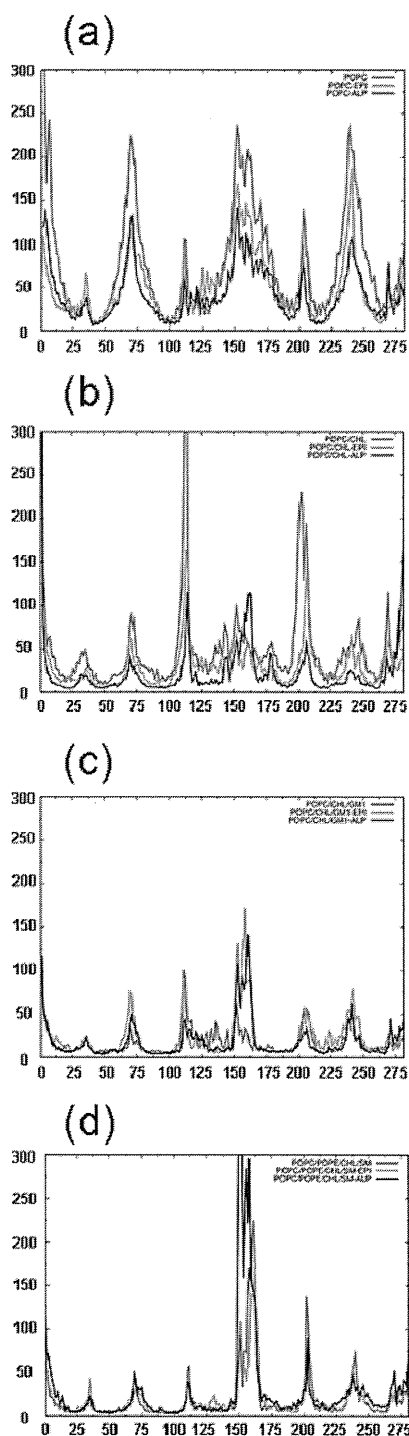
Fig. 2. Superimposition of B-Factor Values for All Residues of β_2AR in apo-Form and the Agonist- or the Antagonist-Bound Form

(a) Pure POPC bilayer, (b) POPC/CHL bilayer, (c) POPC/CHL/GM1 bilayer, and (d) POPC/POPE/CHL/SM mixed bilayer. B-Factor values were obtained from the trajectories for the 100 ns.

network between ligand and receptor. In case of alprenolol (Fig. 3d, Figs. S3, S4), it interacted with Asp113[3.32] but no interaction with Ser203[5.42] and Ser207[5.46]. Hence, the inverse agonist and/or antagonist will be not involved in the movement of helix5, which is compatible with the previous computational study.[61] The interactions between ligand (epinephrine or alprenolol) and β_2AR (Figs. 3c, d) indicated that a stable interaction maintained in the simulation.

Ionic Lock Formation It is important to examine the

activation of β_2AR in terms of the contribution of the intracellular amino acid residues to the formation of ionic lock (Fig. 4). The ionic lock was continuously formed in pure POPC and POPC/POPE/CHL/SM mixed membrane containing apo-, and epinephrine- or alprenolol-bound β_2ARs. In the simulations a, a′, a″ and d, d′, d″, β_2AR maintained a formation of ionic lock and the intracellular ends of helix3 and helix6 made a close network with each other (Fig. 4). Arg131[3.50] and Glu268[6.30] interacted with each other via salt bridge during the MD simulation. In a β_2AR crystal structure; PDB code: 2RH1, $C_\alpha-C_\alpha$ and N–O distances of Arg131[3.50] and Glu268[6.30] were 11.2 Å and 9.9 Å respectively, but typical distances of the inactive rhodopsin structures were ca. 8.8 Å and ca. 2.8 Å. The $C_\alpha-C_\alpha$ and N–O distances were ca. 9.5 Å and ca. 3.0 Å throughout the 100 ns simulations in a–a″ and d–d″ (Fig. 4). Both of these simulations showed that the ionic lock was formed and helix3 and helix6 were close to each other. The N–O distance in Fig. 4 shows two pairs of lines, one pair represents NH1 to OE1 and OE2 distances and another one represents NH2 to OE1 and OE2 distances. The distances of the two lines in the respective pairs were observed to synchronize with each other. The side chain atoms of Arg131[3.50] and Glu268[6.30] fluctuated during the simulation while they always maintained the formation of ionic lock. No noticeable difference was observed among apo-, epinephrine- and alprenolol-bound β_2AR.

The apo-, and epinephrine- or alprenolol-bound β_2AR in POPC/CHL bilayer in simulations b, b′ and b″ showed the break of the ionic lock (Fig. 4). The ionic lock was broken frequently in these three simulations. The N–O distances show no clear separation in four lines. The displacement of the side chain atoms of Arg131[3.50] and Glu268[6.30] are large compared to the simulations with other type of lipid membrane. The apo-, and epinephrine- or alprenolol-bound β_2ARs in the POPC/CHL/GM1 bilayer in simulations c, c′ and c″ showed the instability of the ionic lock (Fig. 4). The ionic lock distance was frequently enlarged compared with simulations a–a″ and d–d″. The present findings suggest that the ionic lock distance depends on the lipid compositions.

Characteristic Conformational Changes in the Side Chain Residues The conformational change of side chain will affect on Gα protein bound with β_2AR. Hence we analyzed the conformation of the side chains at the intracellular part of β_2AR, especially for three residues Thr68[2.39], Asp130[3.49] and Arg131[3.50] that are involved in the binding to Gα protein. The conformations of these three residues are similar among all the models. The distances between two of these three residues are represented in Figs. S5 and S6 of Supplementary Information. The $C_\alpha-C_\alpha$ and N–O distances give the almost similar kinds of results in apo-, and epinephrine- or alprenolol-bound β_2AR in all models. We observed the $C_\alpha-C_\alpha$ and N–O distances between Thr68[2.39] and Asp130[3.49] in all simulations. The distances were ca. 7.5 Å and 3–6 Å in a–a″, c–c″ and d–d″ (Fig. S5). In contrast, the distances were ca. 9.5 Å and 5–8.5 Å in the CHL bilayer simulations in b–b″. We also evaluated the $C_\alpha-C_\alpha$ and N–O distances between Thr68[2.39] and Arg131[3.50] in all the simulations. The distances were ca. 8.5 Å and 4 Å in a–a″, c–c″ and d–d″ (Fig. S6), but these distances were 9–10.5 Å and 4–6 Å in CHL containing membrane in b–b″. These changes in distance are similar to Fig. 4. In contrast, Lys267[6.29] and Asp331[7.58] showed a different conformational change among all the models (Fig. 5). The
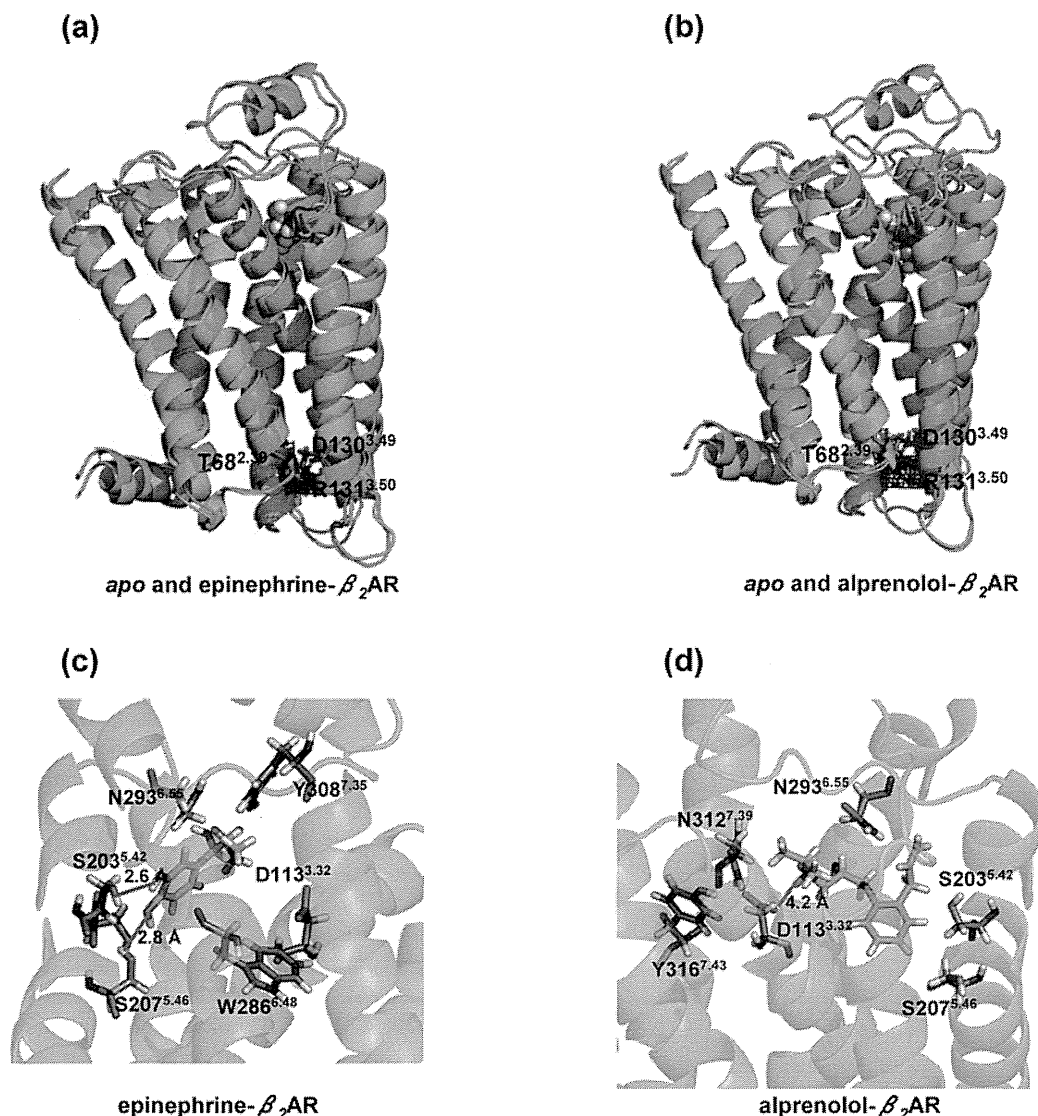
(a)

apo and epinephrine-β_2AR

(b)

apo and alprenolol-β_2AR

(c)

epinephrine-β_2AR

(d)

alprenolol-β_2AR

Fig. 3. (a), (b) Superimposition of the Average Structure of Ligand-Bound β_2AR (Cyan) on That of the *apo* One (Green), Obtained in the POPC/POPE/CHL/SM Mixed Membrane

The interaction domain with Gα protein is shown by blue mesh at the intracellular part of the receptor. (c), (d) Close view of the ligand, epinephrine or alprenolol, binding site of β_2AR in POPC/POPE/CHL/SM mixed bilayer. (Color images were converted into gray scale.)

distance between Lys267[6.29] and Asp331[7.58] was relatively short in *apo*- and alprenolol-bound β_2AR in all models whereas the distances became long in the epinephrine-bound β_2AR. Judging from these N–O distances, we concluded that the interaction was stably maintained between Lys267[6.29] and Asp331[7.58] in a and a″. In contrast, this interaction was often broken in a′ for the epinephrine-bound β_2AR. The N–O distance between Lys267[6.29] and Asp331[7.58] was occasionally maintained in b and b″, c and c″, d and d″ and the interaction was almost broken in b′, c′ and d′. Therefore, the distance between Lys267[6.29] and Asp331[7.58] will be one of the important indices that varies depending on the presence and the absence of antagonist.

Distribution of Lipid Molecules The distribution of lipid molecules were analyzed using the trajectories acquired from the last 30 ns MD simulation (Fig. S7). The lipid molecules, which are located near around β_2AR, showed sharp distributions, whereas distributions became broad for the lipid molecules that are apart from β_2AR. The sharpness in distribution will be due to the interaction between lipid molecules and

β_2AR. The lipid molecule, CHL, is found to be distributed heterogeneously in all the models (Fig. S7). Superimpositions of the distribution of lipid molecules in *apo*- and epinephrine- or alprenolol-β_2AR for the respective membrane models are shown in Fig. S8. In case of POPC/POPE/CHL/SM mixed membrane, two CHLs marked by red circle always stay at the same position during last 30 ns MD simulations (Fig. 6a). This position is the location between the helix4 and helix5 of β_2AR. Figure 6b shows the top view of CHL distributions around β_2AR and the CHLs colored red are bound to β_2AR. CHL has a highly hydrophobic part. In the upper and lower leaflets of the lipid membrane, two CHLs mainly interact with the nonpolar hydrophobic residues of Ala198[5.37], Ala202[5.41], Val206[5.45], Pro168[4.60], Ile214[5.53], Val126[3.45] and Val129[3.48] (Fig. 6c). The CHL in the upper leaflet interacts with Ala198[5.37], Ala202[5.41], and Val206[5.45] and Pro168[4.60]. The CHL in the lower leaflet interacts with Val206[5.45], Ile214[5.53] and Val126[3.45], Val129[3.48]. Hence the hydrophobic interaction tightly connects CHL molecule to helix5 of β_2AR.
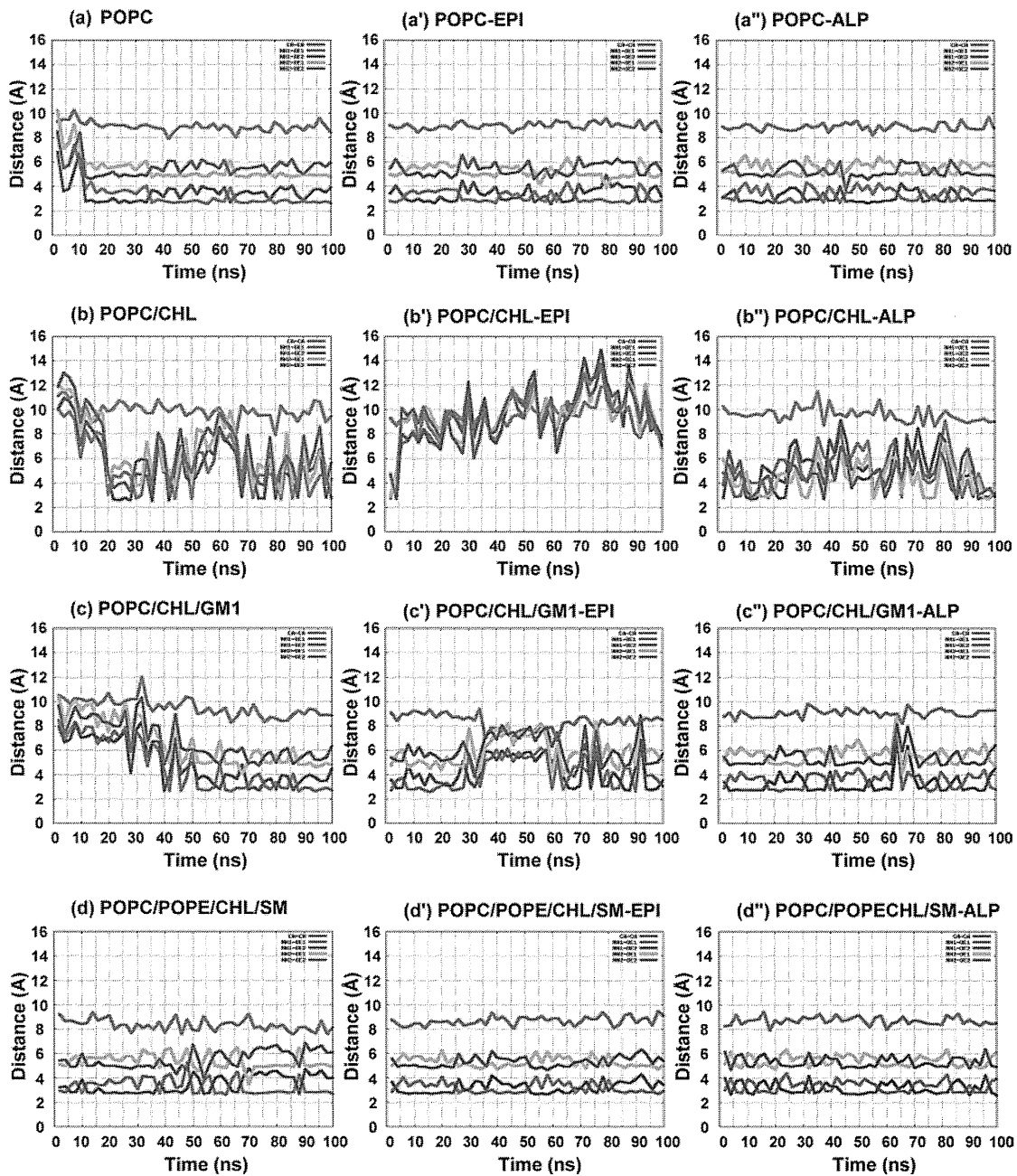
Fig. 4. Ionic Lock Distance in β_2AR Receptor

$C\alpha$–$C\alpha$ (red) and N–O (NH1-OE1: blue; NH1-OE2: magenta; NH2-OE1: cyan; NH2-OE2: brown) distances were measured for 100 ns in MD simulations. apo-β_2AR and the agonist epinephrine- or the antagonist alprenolol-bound β_2AR in pure POPC (a, a', a''), POPC/CHL/GM1 (c, c', c'') and POPC/POPE/CHL/SM (d, d', d'') keep the ionic lock formation while the ionic lock is broken in POPC/CHL (b, b', b''). (Color images were converted into gray scale.)

Discussion

Protein flexibility is closely related to the function of a protein. We have analyzed the residue fluctuation by B-factor analysis. The comparison of B-factor among the simulation models indicated that the flexibility of protein residues in apo form is higher than those in the presence of epinephrine and alprenolol. Protein residues give the smallest fluctuation in the presence of alprenolol, which suggests that alprenolol stabilizes the β_2AR structure. Goetz et al. carried out MD simulation on the agonist isoprenaline- or inverse agonist carazolol-bound β_2AR.[61] Their comparison of B-factor between the isoprenaline- and the carazolol-bound β_2ARs demonstrated that the residue fluctuation was reduced in the presence of carazolol,

which is consistent with our results (Fig. S1, Fig. 2).

Some previous studies have revealed that the binding modes of epinephrine and alprenolol to β_2AR were different.[9,10,62–64] In computational approaches, Simpson et al. carried out MD simulation on the epinephrine-bound β_2AR.[62] In their calculation the hydrogen-bond interactions with epinephrine were observed at Ser203[5.42], Ser207[5.46] and Asp113[3.32], which is compatible with our results (Fig. 3c, Figs. S3, S4). An X-ray crystal analysis suggested the interaction of Ser203[5.42] and Ser207[5.46] with a ligand.[10] In many computational studies on the structure of the agonist-bound and the inverse agonist/antagonist-bound β_2ARs, an agonist was found to make hydrogen-bonds with receptor through the residues of Ser203[5.42],
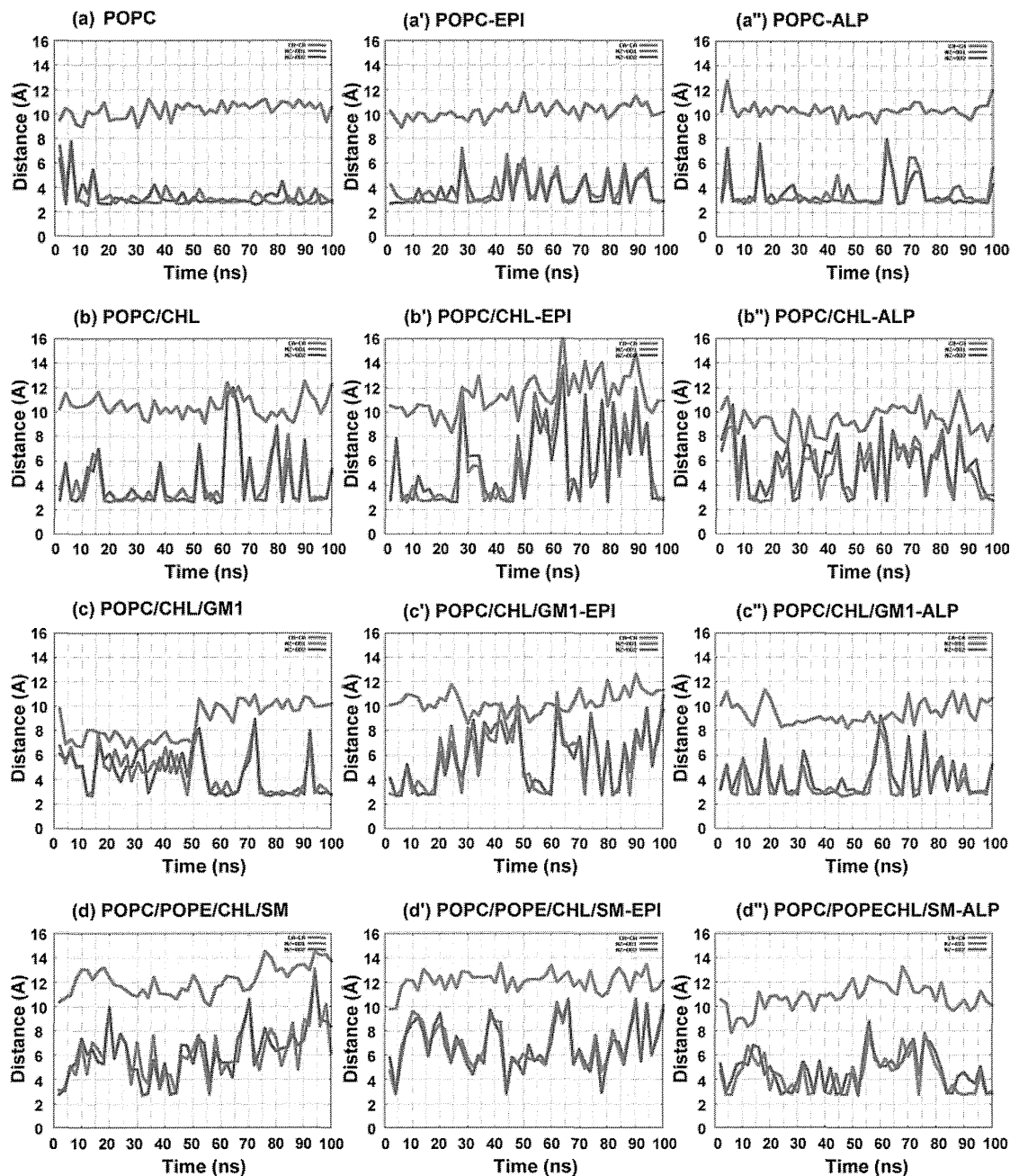
Fig. 5.   Distances between the Side Chain of Lys267$^{6.29}$ and Asp331$^{7.58}$ at the Intracellular Part of β_2AR

Cα–Cα (red) and N–O (NZ-OD1: blue; NZ-OD2: magenta) distances were monitored all through 100ns of MD simulation. (Color images were converted into gray scale.)

Ser207$^{5.46}$ and Asp113$^{3.32}$.[63,64] In contrast, the inverse agonist/antagonist bound to β_2AR was shown to make the hydrogen-bond network with Asp113$^{3.32}$ and not to establish the hydrogen-bonds with Ser203$^{5.42}$ and Ser207$^{5.46}$,[9] which is also consistent with our current findings (Fig. 3d, Figs. S3, S4).

The ionic lock formation of GPCR in lipid membrane has already been studied in simulation and suggested to play an important role in the activation of GPCR.[6,65] About 70% of GPCRs of the rhodopsin family contain the E(D)RY(W) motif on helix3. Arg135$^{3.50}$ of the conserved motif makes an intrahelical salt bridge to the neighboring Glu134$^{3.49}$. Arg135$^{3.50}$ also interacts with Glu247$^{6.30}$ strongly. Further, Glu249$^{6.32}$ interacts with the backbone NH of Lys311$^{7.58}$ at the kink from helix7 to the small cytoplasmic helix8. During the activation

of rhodopsin, the interhelical interactions between Arg135$^{3.50}$ and Glu247$^{6.30}$, and between Glu249$^{6.32}$ and Lys311$^{7.58}$ were observed to be broken.[65] The disruption of the intrahelical salt bridge between Glu134$^{3.49}$ and Arg135$^{3.50}$ at the cytoplasmic terminus of helix3 was proposed to be a key factor for the transition to the active conformation.[6,65]

An important difference between the crystallographic structures of rhodopsin[26–28] and β_2AR[5,8,45,66] bound with the partial inverse agonist carazolol and timolol is the disruption of the ionic lock. The β_2AR structures lack the interhelical interactions between homologous residues Arg131$^{3.50}$ and Glu268$^{6.30}$, and between Lys270$^{6.32}$ and Asp331$^{7.58}$. Dror *et al.* carried out MD simulation on a carazolol-bound β_2AR embedded in pure POPE lipid bilayer.[6] They showed that the C$_\alpha$–C$_\alpha$ distance

(a)

POPC/CHL/SM/POPE--apo   POPC/CHL/SM/POPE--EPI   POPC/CHL/SM/POPE--ALP

(b)

(c)

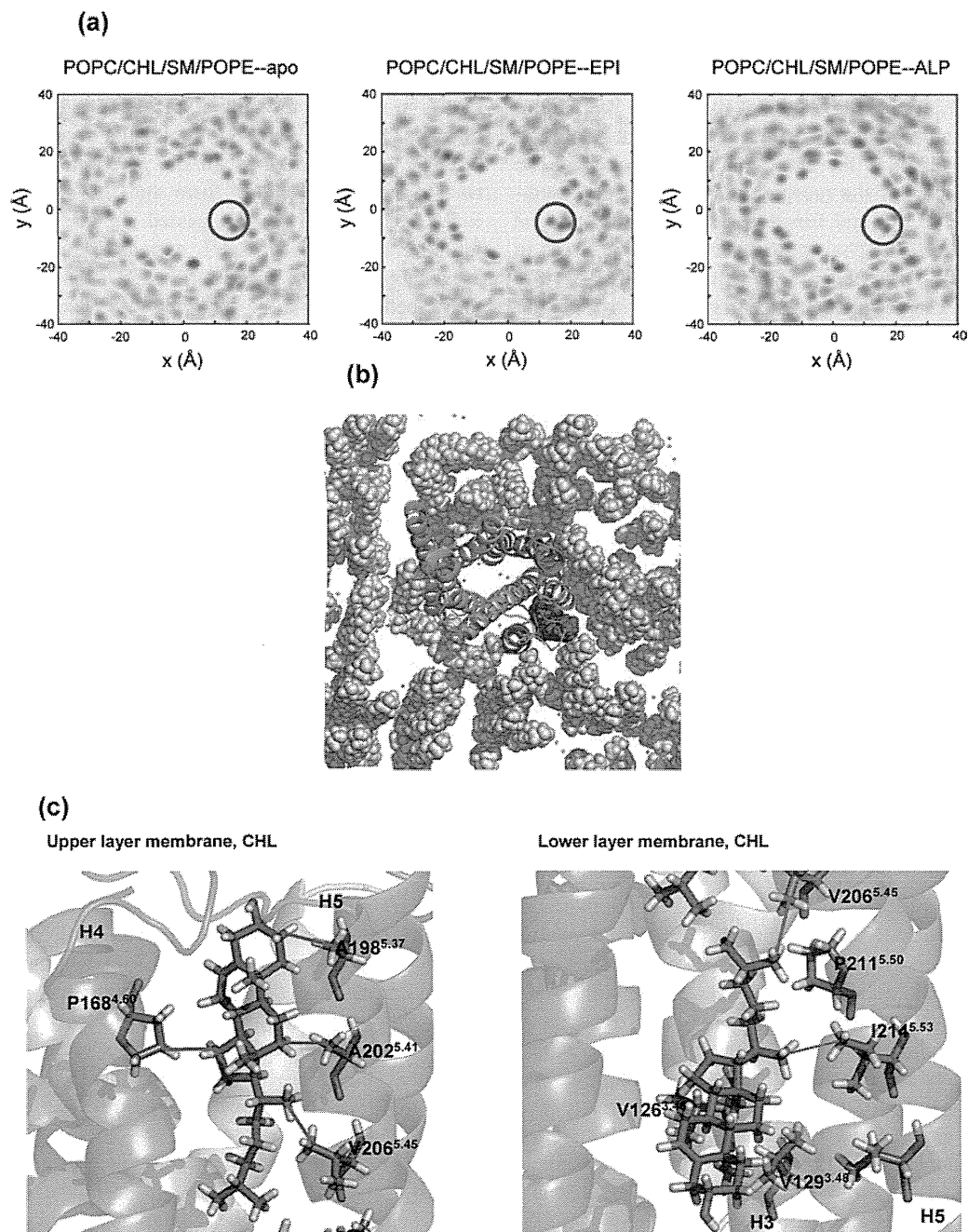Upper layer membrane, CHL   Lower layer membrane, CHL

Fig. 6.   (a) Distribution of the Lipid Molecules for POPC (Green), POPE (Blue), CHL (Red) and SM (Cyan)

Red circle indicates the area that CHL molecules always stay during the last 30ns of MD simulation. (b) Close view of CHL distribution around GPCR, in which the CHL colored red is always bound to GPCR. (c) Hydrophobic interaction between the CHL and GPCR in the upper and the lower leaflets of the lipid membrane. (Color images were converted into gray scale.)

was below 9.5 Å for 91% of the simulation time. According to their results, the ionic lock was stably maintained between the backbones of $Arg131^{3.50}$ and $Glu268^{6.30}$ for the inverse agonist bound β_2AR. This finding is consistent with our results using the pure POPC bilayer. But the intrahelical salt bridge between two adjacent residues $Asp130^{3.49}$ and $Arg131^{3.50}$ appear to be preserved and it stabilizes the inactivated form of the receptor. Furthermore, intracellular ends of helices 3 and 6 are substantially far apart from each other compared with those in rhodopsin.[6] The disruption of the ionic lock was previously suggested to be the crucial step for the GPCR activation. Some mutagenesis studies indicated that the mutations of the residues related to the ionic lock in β_2AR and those of

homologous residues in rhodopsin-family GPCRs resulted in a continuous receptor activation.[31–33,65] In spite of the above suggestion, the ionic lock may be not only major factor in GPCR activation because β_2AR has the broken ionic lock in the crystallographic structures.

In the inactive state of β_2AR, $Lys270^{6.32}$ and $Asp331^{7.58}$ were suggested not to interact with each other in contrast to the interaction between the homologous residues; $Glu249^{6.32}$ and $Lys311^{7.58}$, in the inactive state of rhodopsin.[65] In our results we found that another residue, $Lys267^{6.29}$ kept an adequate distance to $Asp331^{7.58}$ in apo- and alprenolol-bound β_2AR in all calculation models. In the epinephrine-bound β_2AR structures, this distance became noticeably larger in all models, which

suggests the presence of a different kind of salt bridge in the inactive form of β_2AR.

The transmembrane receptors are in contact with the membrane lipid bilayer, which suggests that membrane has an important influence on receptor structure and function.[67] Hence, it is necessary to analyze the effect of lipid composition on the structural stability of the receptor. As well as other membrane proteins,[14] the optimal function of GPCR will depend on the lipid environment. The significance of specific lipids in the function of GPCR has been demonstrated in a variety of studies.[68,69] For example, the presence of phosphatidylethanolamine (PE) was shown to modulate the activation of GPCR.[68] In addition, the presence of phospholipids with unsaturated fatty acids in the membrane is required for efficient signaling of rhodopsin.[69] Similar to other lipid molecules, CHL is also required for the optimal function of membrane proteins.[67] The lipid-receptor interactions, especially CHL-receptor interaction, is involved in the modification of conformation and function of several GPCR family proteins.[15] CHL is distributed heterogeneously in domains or pools of biological and artificial membranes[70] and believed to be important for the maintenance of membrane structure. CHL modulates the conformation and the function of membrane proteins by a direct molecular interaction with the receptor[71] or due to the alteration of the membrane physical properties induced by the presence of CHL.[67,72,73] For example, CHL is directly bound to the sterol regulatory element binding protein cleavage activating protein (SCAP), which is a large polytopic membrane protein, thereby CHL induces a conformational change in SCAP.

The CHL-receptor interactions have extensively been studied in the case of rhodopsin. Due to the increase of the amount of CHL, rhodopsin shifted itself to the inactive conformation.[74] Molecular dynamic simulation with rhodopsin in a membrane containing CHL and unsaturated phospholipids suggested the direct interaction between rhodopsin and CHL[75] and hence the enhancement of the stability of the receptor in the membrane. Further, CHL is required for keeping a high binding affinity between ligand and receptor. For example, the efficiency of ligand binding to the cholecystokinin receptor was reported to be reduced by the lowering of the concentration of CHL in membrane.[76] The importance of CHL in membrane for the ligand binding was also suggested in subtype 2 galanin (GalR2) and oxytocin receptor.[77,78] Moreover, CHL-receptor interaction was also found in case of β_2AR. A recent X-ray crystal analysis suggested that CHL molecules were tightly bound to β_2AR[45] and CHL seemed to be an important component for crystallization of the receptor. These findings indicate that CHL composes a specific interaction with β_2AR and promotes the enzymatic functions for ligand binding, receptor-G-protein interaction, and/or downstream signal transduction.[79] Hanson et al. provided the crystal structure of β_2AR bound with both CHL and a partial inverse agonist timolol and showed that CHL was bound at a shallow surface groove formed by segments of helices 1, 2, 3, and 4.[8] CHL was shown to enhance the thermal stability of β_2AR, by forming many intermolecular interactions through van der Waals interactions or hydrogen bonding to β_2AR helix. For example, Tyr70$^{2.41}$ makes the van der Waals interaction with ring A of CHL and a hydrogen bond to Arg151$^{4.43}$ in β_2AR.[8] A recent study proposed a characteristic amino acid sequence, named as cholesterol recognition/interaction amino acid consensus

(CRAC) motif, which is the dominant region interacting with CHL and observed in three representative GPCRs of rhodopsin, β_2AR and serotonin$_{1A}$ receptor. β_2AR presents CRAC motifs in transmembrane helix5; residues 231–221, and helix7; residues 324–328.[80] In our molecular dynamics study, CHL binding was observed in all the β_2AR in apo- and epinephrine- or alprenolol-bound form and the contribution of CHL for β_2AR stability was suggested. In our simulations except for pure POPC model, CHL appeared to be distributed heterogeneously in the membranes and a specific CHL-binding to the helices 3, 4 and 5 in β_2AR was observed in the simulations c–d." CHL molecules mainly interacted with the hydrophobic residues such as Ala198$^{5.37}$, Ala202$^{5.41}$, Val206$^{5.45}$ and Ile214$^{5.53}$, with its principle molecular axis almost parallel to the membrane normal direction. The change of the distances between CHL and these residues were monitored for the last 30 ns of MD simulation (Fig. S9). The fluctuation of these distances was small during the simulation, which suggested that the hydrophobic interaction was stable. In order to evaluate the interaction from the quantitative viewpoint, the shape-complementarity between CHL and β_2AR was measured. The shape-complementarity was calculated to be was 0.68. This value is higher than those of the antigen-antibody interfaces, while slightly lower than those of the interfaces between proteases and their inhibitors.[81] Therefore, the molecular shape of CHL is concluded to be well compatible with the helix4 and helix5 region of β_2AR.

Conclusion

The influence of the lipid composition on the structural conformation of one kind of GPCR protein, β_2AR, was investigated by performing molecular dynamics simulations. Four types of lipid membranes, pure POPC, POPC/CHL, POPC/CHL/GM1 and POPC/POPE/CHL/SM containing three kinds of β_2AR; apo- and the agonist epinephrine- or the antagonist alprenolol-bound form, were employed for 100 ns simulation and the computational results were compared. This work presented the following findings. (1) The stability of the ionic lock formation between Arg131$^{3.50}$ and Glu268$^{6.30}$ varies depending on the difference of the lipid component of membrane. (2) The side chain interaction between Lys267$^{6.29}$ and Asp331$^{7.58}$ became strong in apo- and the alprenolol-bound β_2AR, compared with the epinephrine-bound β_2AR in pure POPC membrane. (3) A stable hydrophobic interaction was observed between CHL and the receptor at the transmembrane helix5 in POPC/CHL/GM1 and POPC/POPE/CHL/SM membranes. CHL is specifically bound at the position between helix4 and helix5 in β_2AR.

References

1) Audet M., Bouvier M., *Nat. Chem. Biol.*, **4**, 397–403 (2008).
2) Lefkowitz R. J., *Biochim. Biophys. Acta*, **1768**, 748–755 (2007).
3) Jones S. M., Hiller F. C., Jacobi S. E., Foreman S. K., Pittman L. M., Cornett L. E., *BMC Pharmacol.*, **3**, 15 (2003).
4) Rasmussen S. G., DeVree B. T., Zou Y., Kruse A. C., Chung K. Y.,

Kobilka T. S., Thian F. S., Chae P. S., Pardon E., Calinski D., Mathiesen J. M., Shah S. T., Lyons J. A., Caffrey M., Gellman S. H., Steyaert J., Skiniotis G., Weis W. I., Sunahara R. K., Kobilka B. K., *Nature* (London), **477**, 549–555 (2011).

5) Rosenbaum D. M., Cherezov V., Hanson M. A., Rasmussen S. G., Thian F. S., Kobilka T. S., Choi H. J., Yao X. J., Weis W. I., Stevens R. C., Kobilka B. K., *Science*, **318**, 1266–1273 (2007).

6) Dror R. O., Arlow D. H., Borhani D. W., Jensen M. Ø., Piana S., Shaw D. E., *Proc. Natl. Acad. Sci. U.S.A.*, **106**, 4689–4694 (2009).

7) Dixon R. A., Kobilka B. K., Strader D. J., Benovic J. L., Dohlman H. G., Frielle T., Bolanowski M. A., Bennett C. D., Rands E., Diehl R. E., Mumford R. A., Slater E. E., Sigal I. S., Caron M. G., Lefkowitz R. J., Strader C. D., *Nature* (London), **321**, 75–79 (1986).

8) Hanson M. A., Cherezov V., Griffith M. T., Roth C. B., Jaakola V. P., Chien E. Y., Velasquez J., Kuhn P., Stevens R. C., *Structure*, **16**, 897–905 (2008).

9) Wacker D., Fenalti G., Brown M. A., Katritch V., Abagyan R., Cherezov V., Stevens R. C., *J. Am. Chem. Soc.*, **132**, 11443–11445 (2010).

10) Rosenbaum D. M., Zhang C., Lyons J. A., Holl R., Aragao D., Arlow D. H., Rasmussen S. G., Choi H. J., Devree B. T., Sunahara R. K., Chae P. S., Gellman S. H., Dror R. O., Shaw D. E., Weis W. I., Caffrey M., Gmeiner P., Kobilka B. K., *Nature* (London), **469**, 236–240 (2011).

11) Dror R. O., Arlow D. H., Maragakis P., Mildorf T. J., Pan A. C., Xu H., Borhani D. W., Shaw D. E., *Proc. Natl. Acad. Sci. U.S.A.*, **108**, 18684–18689 (2011).

12) Chini B., Parenti M., *J. Mol. Endocrinol.*, **32**, 325–338 (2004).

13) Pike L. J., *J. Lipid Res.*, **44**, 655–667 (2003).

14) Pucadyil T. J., Chattopadhyay A., *Prog. Lipid Res.*, **45**, 295–333 (2006).

15) Burger K., Gimpl G., Fahrenholz F., *Cell. Mol. Life Sci.*, **57**, 1577–1592 (2000).

16) Lingwood D., Simons K., *Science*, **327**, 46–50 (2010).

17) Mori K., Hata M., Neya S., Hoshino T., *Chem. Bio. Info. J.*, **4**, 15–26 (2004).

18) Madison K. C., Wertz P. W., Strauss J. S., Downing D. T., *J. Invest. Dermatol.*, **87**, 253–259 (1986).

19) Ingraham L. M., Burns C. P., Boxer L. A., Baehner R. L., Haak R. A., *J. Cell Biol.*, **89**, 510–516 (1981).

20) Brügger B., Glass B., Haberkant P., Leibrecht I., Wieland F. T., Kräusslich H. G., *Proc. Natl. Acad. Sci. U.S.A.*, **103**, 2641–2646 (2006).

21) Winterbourn C. C., Batt R. D., *Biochim. Biophys. Acta*, **202**, 1–8 (1970).

22) Farrens D. L., Altenbach C., Yang K., Hubbell W. L., Khorana H. G., *Science*, **274**, 768–770 (1996).

23) Sheikh S. P., Zvyaga T. A., Lichtarge O., Sakmar T. P., Bourne H. R., *Nature* (London), **383**, 347–350 (1996).

24) Jensen A. D., Guarnieri F., Rasmussen S. G., Asmar F., Ballesteros J. A., Gether U., *J. Biol. Chem.*, **276**, 9279–9290 (2001).

25) Ballesteros J. A., Weinstein H., *Methods Neurosci.*, **25**, 366–428 (1995).

26) Palczewski K., Kumasaka T., Hori T., Behnke C. A., Motoshima H., Fox B. A., Le Trong I., Teller D. C., Okada T., Stenkamp R. E., Yamamoto M., Miyano M., *Science*, **289**, 739–745 (2000).

27) Okada T., Sugihara M., Bondar A. N., Elstner M., Entel P., Buss V., *J. Mol. Biol.*, **342**, 571–583 (2004).

28) Li J., Edwards P. C., Burghammer M., Villa C., Schertler G. F. X., *J. Mol. Biol.*, **343**, 1409–1438 (2004).

29) Altenbach C., Kusnetzow A. K., Ernst O. P., Hofmann K. P., Hubbell W. L., *Proc. Natl. Acad. Sci. U.S.A.*, **105**, 7439–7444 (2008).

30) Scheerer P., Park J. H., Hildebrand P. W., Kim Y. J., Krauss N., Choe H. W., Hofmann K. P., Ernst O. P., *Nature* (London), **455**, 497–502 (2008).

31) Ballesteros J. A., Jensen A. D., Liapakis G., Rasmussen S. G., Shi L., Gether U., Javitch J. A., *J. Biol. Chem.*, **276**, 29171–29177 (2001).

32) Greasley P. J., Fanelli F., Rossier O., Abuin L., Cotecchia S., *Mol. Pharmacol.*, **61**, 1025–1032 (2002).

33) Angelova K., Fanelli F., Puett D., *J. Biol. Chem.*, **277**, 32202–32213 (2002).

34) Shapiro D. A., Kristiansen K., Weiner D. M., Kroeze W. K., Roth B. L., *J. Biol. Chem.*, **277**, 11441–11449 (2002).

35) Yao X., Parnot C., Deupi X., Ratnala V. R., Swaminath G., Farrens D., Kobilka B., *Nat. Chem. Biol.*, **2**, 417–422 (2006).

36) West G. M., Chien E. Y., Katritch V., Gatchalian J., Chalmers M. J., Stevens R. C., Griffin P. R., *Structure*, **19**, 1424–1432 (2011).

37) Tikhonova I. G., Best R. B., Engel S., Gershengorn M. C., Hummer G., Costanzi S., *J. Am. Chem. Soc.*, **130**, 10141–10149 (2008).

38) Spijker P., Vaidehi N., Freddolino P. L., Hilbers P. A. J., Goddard W. A. 3rd, *Proc. Natl. Acad. Sci. U.S.A.*, **103**, 4882–4887 (2006).

39) Huber T., Menon S., Sakmar T. P., *Biochemistry*, **47**, 11013–11023 (2008).

40) Sato Y., Hata M., Neya S., Hoshino T., *J. Phys. Chem. B*, **110**, 22804–22812 (2006).

41) Khelashvili G., Mondal S., Andersen O. S., Weinstein H., *J. Phys. Chem. B*, **114**, 12046–12057 (2010).

42) Visiers I., Ballesteros J. A., Weinstein H., *Methods Enzymol.*, **343**, 329–371 (2002).

43) Filizola M., Weinstein H., *Curr. Opin. Drug Discov. Devel.*, **8**, 577–584 (2005).

44) Weinstein H., *AAPS J.*, **7**, E871–E884 (2005).

45) Cherezov V., Rosenbaum D. M., Hanson M. A., Rasmussen S. G., Thian F. S., Kobilka T. S., Choi H. J., Kuhn P., Weis W. I., Kobilka B. K., Stevens R. C., *Science*, **318**, 1258–1265 (2007).

46) Li H., Robertson A. D., Jensen J. H., *Proteins*, **61**, 704–721 (2005).

47) Gilson M. K., Sharp K. A., Honig B. H., *J. Comput. Chem.*, **9**, 327–335 (1988).

48) Momany F. A., Rone R., *J. Comput. Chem.*, **13**, 888–900 (1992).

49) Feller S. E., MacKerell A. D., *J. Phys. Chem. B*, **104**, 7510–7515 (2000).

50) Humphrey W., Dalke A., Schulten K., *J. Mol. Graph.*, **14**, 33–38 (1996).

51) Mori K., Mahmood M. I., Neya S., Matsuzaki K., Hoshino T., *J. Phys. Chem. B*, **116**, 5111–5121 (2012).

52) Phillips J. C., Braun R., Wang W., Gumbart J., Tajkhorshid E., Villa E., Chipot C., Skeel R. D., Kalé L., Schulten K., *J. Comput. Chem.*, **26**, 1781–1802 (2005).

53) Imai Y., Liu X., Yamagishi J., Mori K., Neya S., Hoshino T., *J. Mol. Graph. Model.*, **29**, 461–469 (2010).

54) Case D. A., Darden T. A., Cheatham T. E. III, Simmerling C. L., Wang J., Duke R. E., Luo R., Crowley M., Walker R. C., Zhang W., Merz K. M., Wang B., Hayik S., Roitberg A., Seabra G., Kolossvary I., Wong K. F., Paesani F., Vanicek J., Wu X., Brozell S. R., Steinbrecher T., Gohlke H., Yang L., Tan C., Mongan J., Hornak V., Cui G., Mathews D. H., Seetin M. G., Sagui C., Babin V., Kollman P. A., "AMBER11 University of California," San Francisco (2010).

55) Zoete V., Michielin O., Karplus M., *J. Mol. Biol.*, **315**, 21–52 (2002).

56) Mori K., Hata M., Neya S., Hoshino T., *J. Am. Chem. Soc.*, **127**, 15127–15137 (2005).

57) Katritch V., Reynolds K. A., Cherezov V., Hanson M. A., Roth C. B., Yeager M., Abagyan R., *J. Mol. Recognit.*, **22**, 307–318 (2009).

58) de Graaf C., Rognan D., *J. Med. Chem.*, **51**, 4978–4985 (2008).

59) Daniel R. M., Dunn R. V., Finney J. L., Smith J. C., *Annu. Rev. Biophys. Biomol. Struct.*, **32**, 69–92 (2003).

60) DeLano W. L., "Pymol software," The DeLano Scientific, San Carlos, CA, U.S.A. (2002).

61) Goetz A., Lanig H., Gmeiner P., Clark T., *J. Mol. Biol.*, **414**, 611–623 (2011).

62) Simpson L. M., Wall I. D., Blaney F. E., Reynolds C. A., *Proteins*, **79**, 1441–1457 (2011).

63) Wolf S., Böckmann M., Höweler U., Schlitter J., Gerwert K., *FEBS*

Lett., **582**, 3335–3342 (2008).

64) Liapakis G., Ballesteros J. A., Papachristou S., Chan W. C., Chen X., Javitch J. A., *J. Biol. Chem.*, **275**, 37779–37788 (2000).

65) Vogel R., Mahalingam M., Lüdeke S., Huber T., Siebert F., Sakmar T. P., *J. Mol. Biol.*, **380**, 648–655 (2008).

66) Rasmussen S. G., Choi H. J., Rosenbaum D. M., Kobilka T. S., Thian F. S., Edwards P. C., Burghammer M., Ratnala V. R., Sanishvili R., Fischetti R. F., Schertler G. F., Weis W. I., Kobilka B. K., *Nature* (London), **450**, 383–387 (2007).

67) Lee A. G., *Biochim. Biophys. Acta*, **1666**, 62–87 (2004).

68) Alves I. D., Salgado G. F., Salamon Z., Brown M. F., Tollin G., Hruby V. J., *Biophys. J.*, **88**, 198–210 (2005).

69) Mitchell D. C., Niu S. L., Litman B. J., *J. Pediatr.*, **143** (Suppl.), S80–S86 (2003).

70) Schroeder F., Woodford J. K., Kavecansky J., Wood W. G., Joiner C., *Mol. Membr. Biol.*, **12**, 113–119 (1995).

71) Gimpl G., Burger K., Fahrenholz F., *Trends Biochem. Sci.*, **27**, 596–599 (2002).

72) Yeagle P. L., *Biochim. Biophys. Acta*, **822**, 267–287 (1985).

73) Ohvo-Rekilä H., Ramstedt B., Leppimäki P., Slotte J. P., *Prog. Lipid Res.*, **41**, 66–97 (2002).

74) Albert A. D., Young J. E., Yeagle P. L., *Biochim. Biophys. Acta*, **1285**, 47–55 (1996).

75) Pitman M. C., Grossfield A., Suits F., Feller S. E., *J. Am. Chem. Soc.*, **127**, 4576–4577 (2005).

76) Harikumar K. G., Puri V., Singh R. D., Hanada K., Pagano R. E., Miller L. J., *J. Biol. Chem.*, **280**, 2176–2185 (2005).

77) Pang L., Graziano M., Wang S., *Biochemistry*, **38**, 12003–12011 (1999).

78) Gimpl G., Burger K., Politowska E., Ciarkowski J., Fahrenholz F., *Exp. Physiol.*, **85** (Spec. No.), 41S–49S (2000).

79) Ben-Arie N., Gileadi C., Schramm M., *Eur. J. Biochem.*, **176**, 649–654 (1988).

80) Jafurulla M., Tiwari S., Chattopadhyay A., *Biochem. Biophys. Res. Commun.*, **404**, 569–573 (2011).

81) Lawrence M. C., Colman P. M., *J. Mol. Biol.*, **234**, 946–950 (1993).

Article

Binding and Aggregation Mechanism of Amyloid β-Peptides onto the GM1 Ganglioside-Containing Lipid Membrane

Tyuji Hoshino,[*,†] Md. Iqbal Mahmood,[†] Kenichi Mori,[†,⊥] and Katsumi Matsuzaki[‡]

[†]Graduate School of Pharmaceutical Sciences, Chiba University, Inohana 1-8-1, Chuo-ku, Chiba 260-8675, Japan
[‡]Graduate School of Pharmaceutical Sciences, Kyoto University, Sakyo-ku, Kyoto 606-8501, Japan

Ⓢ Supporting Information

ABSTRACT: Accumulation and fibril formation of amyloid β (Aβ) peptides onto a ganglioside-rich lipid membrane is a cause of neuro-disturbance diseases. To find out a measure for suppressing the nucleation of a seed for amyloid fibrils, the mechanism of the initial binding of Aβ to the membrane should be clarified. Molecular dynamics simulations were carried out to investigate the adhesion process of Aβ peptides onto a GM1-ganglioside-containing membrane. Multiple computational trials were executed to analyze the probability of occurrence of Aβ binding by using calculation models containing a mixed lipid membrane, water layer, and one, two, or three Aβs. The simulations demonstrated that Aβ peptides approached the membrane after fluctuation in the water layer and occasionally made steady contact with the membrane. Once the steady contact had been established, Aβ was unlikely to be detached from the membrane and developed into a more stably bound form. In the stably bound form, neuraminic acids on the GM1 cluster strongly held the side chain of Lys28 of Aβ, which caused deformation of the C-terminal region of the Aβ. Since the C-terminal region of the Aβ peptide contains many hydrophobic residues, its deformation on the membrane enhances the hydrophobic interaction with other Aβ peptides. The contact region of two Aβs evolved into a parallel β-sheet form, and the third Aβ was observed to be bound to the complex of two Aβs to make a bundle of Aβ peptides. Some key structures involved in the Aβ aggregation on the GM1-containing membrane were deduced from the multiple simulations.
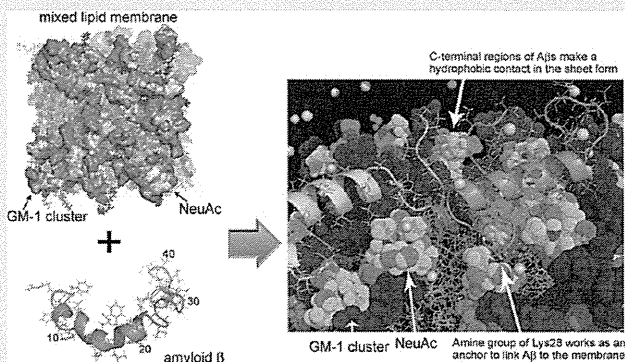
INTRODUCTION

Accumulation of insoluble and filamentous amyloid fibrils is a serious risk factor for some nervous or circulatory diseases. Aggregation of amyloid β (Aβ) peptides has been extensively investigated because of its potential toxicity for amyloid deposition in Alzheimer's disease (AD) and Huntington's disease.[1,2] AD is a severe neurodegenerative disorder that is characterized by deposition of amyloid plaques in the brain.[3] Aβ peptides of 39–43 residues in length are generated from the proteolytic process of amyloid precursor protein (APP) by β- and γ-secretases. The most commonly observed forms of toxic Aβs consist of 40 and/or 42 residues, and the latter is the major component of senile plaque.[4] A comparative study suggested that both $A\beta_{1-40}$ and $A\beta_{1-42}$ exhibited an affinity to the lipid membrane and a similar lipid specificity, but $A\beta_{1-42}$ was more likely to form amyloid fibrils.[5]

Many studies have suggested that the aggregation of toxic Aβ peptides occurs on lipid microdomains containing glycolipids such as ganglioside, sphingomyeline (SM), and cholesterol (Chol) in high concentrations.[6–8] The complex of Aβ and GM1-monosialoganglioside was detected in the brains of patients with AD, suggesting that the Aβ–GM1 complex acts as a seed for the aggregation of Aβ.[9] It has also been proposed that Aβs are likely to be bound to a particular kind of microdomain named the

detergent-insoluble glycoshpingolipid-rich domain (DIG).[9] Several in vitro studies have been carried out to clarify the lipid composition of DIG.[7,8] Matsuzaki et al. demonstrated that a high Chol concentration promoted the formation of GM1 clusters and enhanced Aβ aggregation on the GM1-containig membrane.[10,11] The effect of lipid composition on Aβ binding to GM1-containing bilayers has been examined by preparing several kinds of DIG-mimicking lipid membranes,[10] by changing the component of host lipid membranes such as SM/Chol or POPC,[12] and by substituting the species of ganglioside.[11] These experimental studies suggested that highly condensed GM1 molecules are critical for the formation of the Aβ–GM1 complex. A lipid composition of GM1/SM/Chol = 1:2:2 is one of the adequate membranes providing the DIG-like environment.

In our previous study,[13] 100 ns molecular dynamics (MD) simulations were performed for two kinds of GM1-containing membrane models: one model consisted of GM1, SM, and Chol in a ratio of 1:2:2, and the other model consisted of GM1 and POPC in a ratio of 1:4 for comparison. The simulations showed a marked difference between the two membrane models, GM1
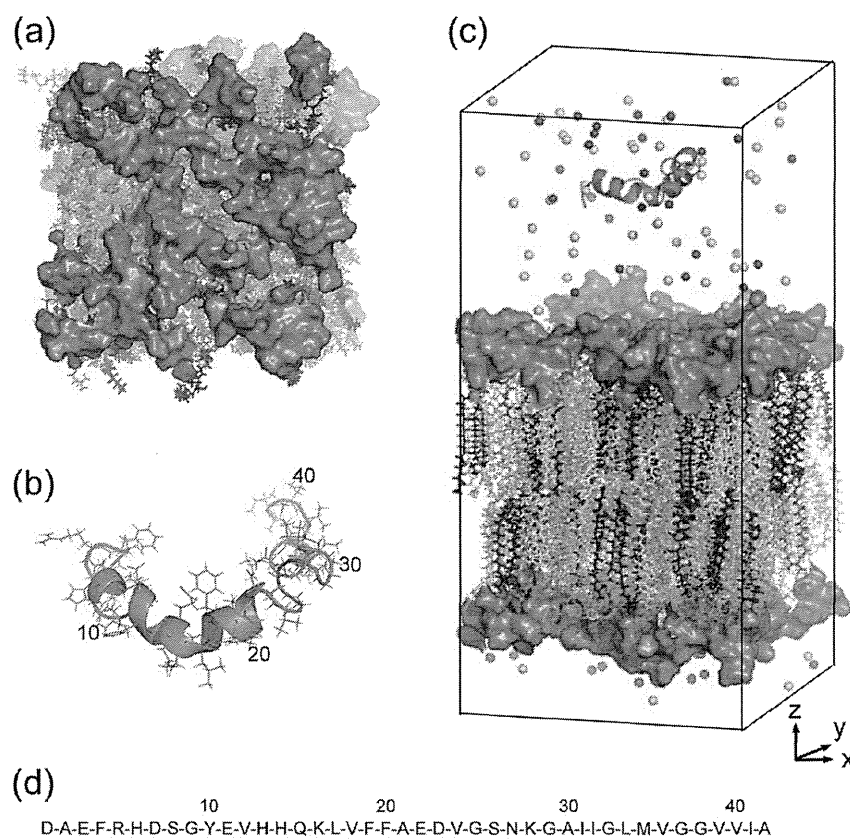
8085

Figure 1. (a) Top view of the equilibrated mixed membrane after 100 ns MD simulation in the lipid composition of GM1:SM:Chol = 1:2:2. GM1 oligosaccharides are depicted in light blue. Acyl chains of GM1, SM, and Chol are colored blue, green, and yellow, respectively. (b) Initial structure of $A\beta_{1-42}$, which is adopted as a starting structure for the first, second, and third $A\beta$s. (c) Computational model for a single $A\beta_{1-42}$ incorporated in the mixed membrane. Sodium and chloride ions are represented by cyan and purple spheres, respectively. The periodic boundary box is indicated by lines. Water molecules are not shown for clarity. (d) Amino acid sequence of $A\beta_{1-42}$. The initial secondary structure of $A\beta_{1-42}$ shown in (b) is indicated at the bottom bar, in which the red area represents a helix and the blue areas represent a turn or sheet.

molecules in the former model being condensed and those in the latter model being scattered. GM1 clusters were formed only on the GM1/SM/Chol membrane.[13] Chol was suggested to play important roles in preventing interdigitation of the membrane and keeping the GM1-ganglioside sphingolipids close enough to form clusters.

Many computational studies have been performed to analyze the behavior of $A\beta$ in an aqueous condition or in the presence of a lipid membrane. Some studies have focused on the structural properties of $A\beta$ peptide.[14−18] It was shown that the C-terminal hydrophobic region plays a critical role in the dimerization,[16] that positively charged amino resides assist the oligomerization,[17] and that four glycine resides promote transformation into the β-sheet form.[18] Several recent works addressed the interaction of $A\beta$ with the lipid membrane.[19−23] However, only a simple lipid membrane consisting of a single kind of lipid molecule such as 1-palmitoyl-2-oleoylphosphatidylcholine (POPC) or dioleoyl-phosphatidylcholine (DOPC) was used in most of those works. The influence of Chol using POPC or DPPC membranes containing Chol has been investigated in only a few studies.[22,23] In experiments, the presence of GM1 ganglioside was already revealed to be critically important for the aggregation of $A\beta$ peptide. Therefore, simulation analysis using a mixed membrane including GM1 ganglioside and Chol is needed.

Clarifying the molecular structures of the $A\beta$−GM1 complex and/or the embryonic stage of $A\beta$ fibrils is important for designing an inhibitor that blocks the generation of the $A\beta$

microaggregate. The final structure of the 100 ns MD simulation for the GM1/SM/Chol model[13] is a good base for analyzing the initial stage of the interaction between $A\beta$ peptides and a biological membrane. Hence, in this study, we carried out multiple MD simulations with incorporation of $A\beta$ molecules into the model system. The computational results will provide a reasonable explanation of why $A\beta$ is stably held by the GM1 cluster and why the $A\beta$ peptides trapped on the membrane become a seed for $A\beta$ fibrils.

■ METHOD

Construction of a Computational Model. The GM1-containing mixed membrane consisted of 48 GM1, 96 SM, and 96 Chol molecules with a molar ratio of 1:2:2. Chemical structures of these lipid molecules are shown in Figure S1 (Supporting Information). The initial coordinates of all of the lipids were extracted from the last snapshot structure of the 100 ns MD simulation of our previous study.[13] The model also contained a water layer and sodium and chloride ions to make the ion concentration equal to 150 mM. The total number of atoms in the model was about 90 000, and the final model size was ca. 70.0 Å × 70.0 Å × 136.0 Å.

The initial atom coordinate of $A\beta_{1-42}$ was extracted from the 11th conformation of PDB code 1Z0Q, which had been determined by solution nuclear magnetic resonance (NMR) spectroscopy.[24] 1Z0Q contains 30 structures,[24] and another code, 1IYT, contains 10 NMR structures.[25] Clustering analysis

with the nearest-neighboring method was applied for both 1Z0Q and 1IYT. Four clusters were obtained for 1Z0Q, and two clusters were obtained for 1IYT (Table S1, Supporting Information). For all of the 40 NMR structures, a 12 ns MD simulation was carried out as a preliminary study. The conformation of Aβ fluctuated during MD simulation, but no marked structural change such as transformation into the β-strand form was observed in any of the simulations. For the reason stated in the footnote of Table S1 (Supporting Information), we selected an Aβ peptide with the 11th conformation of 1Z0Q and inserted it into the midst of the water layer of the GM1-containing membrane model as a starting structure.

Calculation Conditions of MD Simulations. Simulations were performed using the NAMD2.7 program.[26] The calculation procedure was almost the same as that in our previous works.[13,27,28] In short, the production run was carried out at a temperature of 310 K and a pressure of 1 atm. A periodic boundary condition was applied to all of the xyz-directions, and pressure and temperature were kept constant by the Nosé–Hoover Langevin piston method. The cutoff distance of van der Waals and Coulomb forces in a real space was set to 12.0 Å. The integration time step was 2 fs. The particle mesh Ewald method was applied to estimate the effect of long-distance electrostatic force.

Analysis of MD Simulations. The hydrogen bond occupancy was calculated using visual molecular dynamics (VMD).[29] The binding free energy between Aβ peptides was calculated by the MM/GBSA method using the pbsa module of AMBER11[30] in a manner similar to that in the previous studies.[31,32] The secondary structure of Aβ peptides was calculated using the DSSP program.[33] For a better understanding of simulation structures, the positions of some parts of the molecules were transferred to the x-, y-, or z-direction by the length of the periodic boundary box. All of the structures were visualized by PyMol.[34]

RESULTS

Using the GM1/SM/Chol mixed membrane (Figure 1(a)), the movements of Aβ$_{1-42}$ peptides (Figure 1(b)) were investigated through multiple MD simulations with models incorporating one, two, or three Aβs. We carried out 70 ns simulations 10 times for the model with one Aβ, 100 ns simulations 5 times for the model with two Aβs, and 200 ns simulations 2 times for the model with three Aβs. The final structure of the simulation with the one Aβ model was used as the starting structure of the simulation for the two Aβs model, and the final structures of the two Aβs models were used as the starting structure for the three Aβs model (Figure S2, Supporting Information).

Single Aβ Peptide on a GM1-Containing Membrane. To examine the interaction between a single Aβ$_{1-42}$ peptide and the GM1-clustering lipid membrane, 70 ns MD simulations were carried out using the calculation model shown in Figure 1(c). MD simulation will reproduce the dynamic movement of Aβ, which enables us to test the possibility of Aβ binding to the membrane. Since simulation results usually depend on the starting structure, 10 MD simulations, trial I-a–trial I-j, were executed with change in the initial position of Aβ in x and y directions and also rotating Aβ by 180° around the z-axis. Final structures of all of the trials and z-axis changes of the center of mass of the Aβ peptide are shown in Figures S3 and S4 (Supporting Information).

The Aβ peptide initially fluctuated at the water layer in every trial. The terminal regions of Aβ sometimes approached the membrane surface and made contact with the membrane. The contact was soon broken, and Aβ was detached from the membrane in some cases; however, Aβ occasionally continued to be attached to the membrane. Once an Aβ established a steady contact with the membrane, the Aβ was scarcely released from the membrane by itself. Judging from the motion of Aβ during simulation, it seems that there is no special long-distance force to attract Aβ to the membrane.

Table 1 presents a summary of Aβ binding to the membrane for 10 trials. Aβ was firmly bound to the membrane in four trials.

Table 1. Occurrence of Aβ Binding to the Membrane and/or Another Aβ Molecule

number of Aβs in a calculation model	1	2	3
simulation time for one trial (ns)	70	100	200
total number of trials	10	5	2
cases for Aβ bound to membrane[a]	4	3	2
cases for Aβ not bound to membrane[b]	6	2	0
cases for Aβ bound to another Aβ	-	1	2

[a]The occurrence was monitored for the Aβ molecule newly added in the calculation model, for example, the third Aβ in the three Aβs incorporated model. [b]The not bound case includes the situation in which Aβ is just weakly attached to the membrane.

Aβ was weakly attached in two trials, and no Aβ binding was observed for four trials. The Aβ binding, of course, occurred on both sides of the lipid bilayer. The present simulations clearly suggest that Aβ$_{1-42}$ is capable of binding to the GM1-clustering membrane. In the four trials in which Aβ was firmly bound, the Aβ peptide retained the helix conformation in its secondary structure, and the molecular principal axis was almost parallel to the membrane surface (Figure S3, Supporting Information; trials I-a, I-b, I-d, I-i). In the two trials in which Aβ was weakly bound, the helix axis was almost parallel to the membrane in one case (trial I-c), while one terminus stuck in the membrane in another case (trial I-h).

Simulation with Two or Three Aβ Peptides. Extended MD simulations were performed using the calculation model constructed by incorporating an additional Aβ peptide into the final structure of trial I-b. We executed 100 ns MD simulations five times, trials II-a–II-e, with change in the initial position of the second Aβ. The first Aβ was firmly bound to the membrane surface at the starting point. The second Aβ initially fluctuated in the water layer, while the first one was steadily attached to the membrane (Figure S6, Supporting Information). That is, the second Aβ peptide moved randomly, while the motion of the first one was restricted at a local area of the membrane. In the 100 ns MD simulations, the second Aβ was also bound to the membrane in three trials (II-b, II-c, II-d). The second Aβ was bound to the same side of the lipid bilayer as the first one in one trial (II-c), while the second Aβ was bound to the opposite side in two other trials (Figure S5, Supporting Information). In trial II-c, the second Aβ established direct contact with the first one. In contrast, there was no direct interaction between the two Aβs in other trials. This means that the first Aβ has no attractive influence on the second one.

Two 200 ns MD simulations were carried out using the calculation model containing three Aβ peptides. In trial III-a, the third Aβ was incorporated into the final structure of trial II-b, and in trial III-b, Aβ was incorporated into the final structure of trial